J. Fluid Mech. (1992), *vol.* 236, *pp.* 349–383
Printed in Great Britain

Two-dimensional patterns in Rayleigh-Taylor instability of a thin layer

By M. FERMIGIER[1], L. LIMAT[1,2], J. E. WESFREID[1], P. BOUDINET[1] AND C. QUILLIET[1]

[1] Laboratoire d'Hydrodynamique et Mécanique Physique, Ecole Supérieure de Physique et Chimie de Paris, 10, rue Vauquelin, 75231 Paris Cedex 05, France

[2] Laboratoire de Physico-Chimie Théorique, Ecole Supérieure de Physique et Chimie de Paris, 10, rue Vauquelin, 75231 Paris Cedex 05, France

(Received 21 December 1989 and in revised form 2 August 1991)

We study experimentally and theoretically the evolution of two-dimensional patterns in the Rayleigh–Taylor instability of a thin layer of viscous fluid spread on a solid surface. Various kinds of patterns of different symmetries are observed, with possible transition between patterns, the preferred symmetries being the axial and hexagonal ones. Starting from the lubrication hypothesis, we derive the nonlinear evolution equation of the interface, and the amplitude equation of its Fourier components. The evolution laws of the different patterns are calculated at order two or three, the preferred symmetries being related to the non-invariance of the system by amplitude reflection. We also discuss qualitatively the dripping at final stage of the instability.

1. Introduction

In this paper, we report experimental observations of the two-dimensional patterns arising in the gravitational instability of a thin layer of viscous fluid and we derive nonlinear evolution equations for the patterns having different symmetries. The Rayleigh–Taylor instability is a gravitational instability occurring when there is an adverse density stratification in a fluid, i.e. when the resultant acceleration is directed from the heavier towards the lighter fluid (Taylor 1950). If the instability occurs at an interface between two immiscible fluids, it can be understood as a gravitational amplification of capillary waves, the surface tension acting as a stabilizing effect.

In the case of two semi-infinite layers of inviscid fluids, the linear stability analysis (Chandrasekhar 1981) leads to the following dispersion relation for normal modes of deformation of the interface $\zeta(x,t) = \exp[i(qx+\omega t)]$:

$$\omega^2 = \frac{(\rho_1-\rho_2)gq+\gamma q^3}{\rho_1+\rho_2}. \tag{1.1}$$

where g is the net acceleration, $\rho_2(\rho_1)$ is the density of the upper (lower) fluid and γ is the surface tension. The interface is unstable when ω^2 is negative ($\omega = i\sigma$), for wavenumbers q smaller than the capillary wavenumber $q_c = (|\rho_2-\rho_1|g/\gamma)^{\frac{1}{2}}$, the deformation increasing with a time constant $\tau = 1/\sigma$.

The dynamics of the gravitational instability is completely different if the fluids are contained in a porous medium or in a Hele-Shaw cell, cases in which the viscous

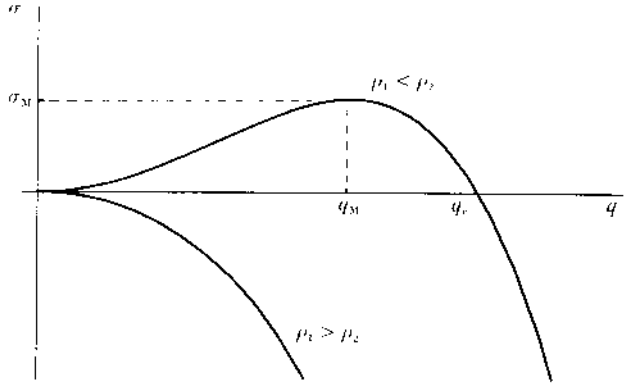

FIGURE 1. Dispersion relationship in the Rayleigh Taylor instability of a thin layer of viscous fluid. The instability occurs when the density ρ_2 of the upper fluid is larger than that of the lower fluid ρ_1.

effects are dominant. The velocity field is then given by Darcy's law and the dispersion relation is

$$\sigma = -k\frac{(\rho_1-\rho_2)gq+\gamma q^3}{\eta_1+\eta_2}. \tag{1.2}$$

where $\eta_1(\eta_2)$ is the viscosity of the upper (lower) fluid and k is the permeability of the medium (for a Hele-Shaw cell of thickness b the permeability is $k = \frac{1}{12}b^2$). When the interface is displaced with a normal average velocity W, the term $|\eta_1/k-\eta_2/k|Wq$ should be added to the destabilizing gravity term $(\rho_1-\rho_2)gq$. If the displaced fluid is the more viscous one, the viscous fingering (Saffman & Taylor 1958) instability is superimposed on the gravitation instability.

The dynamics of the Rayleigh Taylor instability is also governed by viscous effects if one of the fluid layers is very thin, i.e. if the thickness e_0 of the layer is much smaller than the viscous diffusion length $l = (\eta\tau/\rho)^{\frac{1}{2}}$. In this case, the hydrodynamic problem is identical to that encountered in fluctuations of soap films (Vrij 1966). When the wavelength of the instability is large compared to the thickness e_0, the use of the lubrication theory yields the dispersion relation (Vrij 1966; Babchin *et al.* 1983)

$$\sigma = -(e_0^3/3\eta)|(\rho_1-\rho_2)gq^2+\gamma q^4|. \tag{1.3}$$

The relation (1.3) is plotted on figure 1. Again, the perturbations of the interface having a wavenumber smaller than the capillary wavenumber q_c are amplified when $\rho_1 < \rho_2$. The fastest growing mode has a wavenumber $q_m = q_c/\sqrt{2}$, the time constant being inversely proportional to the cube of the thickness of the layer.

The dissipative Rayleigh Taylor instability of thin films has been less explored than the instability of thick layers, where the viscous effects are often neglected, and which has motivated most recent studies (Tan 1986; Jacobs & Catton 1988*a*, *b*; Iooss & Rossi 1989). Yet, the problem of gravitational instability at very low Reynolds number is important in geophysical processes (rising of salt domes, for example), and model laboratory experiments have been performed to investigate this phenomenon (Nettleton 1934; Whitehead & Luther 1975; Whitehead 1988). Recently Yiantsios & Higgins (1989) have performed a careful theoretical and numerical study of the problem of the thin layer. However, their study was restricted to the case of one-dimensional perturbations, and the selection of two-dimensional patterns has received little attention up to now. Whitehead & Luther (1975) have discussed the

development of an hexagonal pattern, but the horizontal extent of their laboratory experiment was too small to investigate the problem of symmetry selection. In addition to the geophysical problems, the instability of thin layers is important in the genesis of two-phase flow in situations of film boiling (Berenson 1962; Sainson 1989; Sainson *et al.* 1990).

In §2 we present our experimental investigations of the thin-layer instability. Different patterns ('rolls', hexagonal, axisymmetric, annular of sixfold symmetry ...) are observed with possible transitions between patterns of different symmetry. We then try to select these patterns by varying the nature of the initial perturbation. At large times, we observe that the axial and hexagonal symmetries are preferred. We also briefly discuss the latest stage of this instability when dripping has occurred.

In §3 we propose a nonlinear analysis of this problem based on the lubrication theory. We derive the nonlinear evolution equation of the interface, and we investigate the growth initiated by small perturbations of this interface. This approach is very similar to that developed by Jacobs & Catton (1988*a*, *b*) in the inviscid case, except that we discuss the nonlinear growth in terms of interactions between Fourier modes (see for instance Busse 1978). The essential property of the system studied is its non-invariance by amplitude reflection, that introduces second order non-linearities in the evolution equations. We present different solutions of the amplitude equations calculated at order two or three, for different initial conditions. In all cases, the second-order nonlinearities favour the growth of the hexagonal and axisymmetric patterns, in agreement with our experimental observations.

Whitehead & Luther (1975) have discussed the influence of second-order nonlinearities in the growth of an hexagonal perturbation of the interface, but in the limit of a vanishing surface tension. Our approach takes into account the capillary effects and allows us to treat higher-order nonlinearities. In addition, we propose a simplified analysis of the annular patterns that avoid treating nonlinear interactions between Bessel functions (§3.5).

2. Experimental

2.1. *Experimental set-up*

An experimental investigation of the Rayleigh Taylor instability requires the preparation of a flat fluid interface in an unstable density stratification. This is done in two steps in our experiment. First, a drop of silicon oil is spread by gravity on a glass plate, yielding a viscous pancake, approximately 30 cm in diameter, and a fraction of millimeter thick. The spreading is very slow and it takes about two days to get a completely spread drop. The spreading has to be stopped because the edge of the pancake becomes irregular owing to surface heterogeneities of the glass plate. Secondly, the glass plate is turned over within a few seconds, a time much smaller than the characteristic time of the gravitational instability (figure 2). Given the physical characteristics of the silicon oil (density $\rho = 0.97\,\mathrm{g/cm^3}$, viscosity $\eta = 1000\,\mathrm{cP}$ and surface tension $\gamma = 21$ dyne/cm) and the typical thickness of the layer $e_0 = 0.2$ mm we can derive the capillary length $\lambda_c = (\gamma/\rho g)^{\frac{1}{2}} = 1.49$ mm. The corresponding wavelength of the fastest growing mode should then be

$$\lambda_M = 2\pi\sqrt{2}\,\lambda_c = 13.2\ \mathrm{mm}. \tag{2.1}$$

The time constant of the instability is obtained from the dispersion relation (1.3) and the associated time constant for λ_M is

$$\tau_M = 12\eta\gamma/e_0^3\rho^2 g^2 = 350\ \mathrm{s}. \tag{2.2}$$

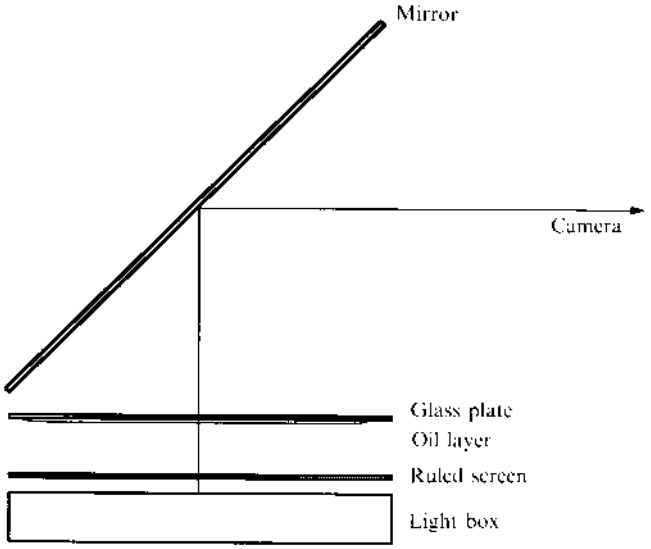

FIGURE 2. Schematic experimental set-up.

The mean thickness e_0 is derived by dividing the total volume of fluid (varying from 15 to 20 cm^3) by the area of the oil pancake. The local thickness was not measured directly but we can infer the thickness variation from the analysis of viscous gravity currents done by Huppert (1982). Huppert obtained similarity solutions for the axisymmetric spreading of a viscous drop neglecting surface tension effects, a reasonable assumption for drops having a radius much larger than the capillary length, except in the vicinity of the drop edge. Using Huppert's solution, which compares quite well to experimental data:

$$e(r,t) = At^{-\frac{1}{3}}(1-Br^2t^{-\frac{1}{3}})^{\frac{1}{3}}. \tag{2.3}$$

where t is the time elapsed from the beginning of spreading. Taking, for example, a volume equal to 20 cm^3 and a spreading time of two days, we get the thickness of the oil layer ranging from 0.227 mm at the centre to 0.166 mm at 15 cm from the centre. Accordingly, the time constant of the instability should increase by approximately a factor of two from the centre to the edge of the layer. This explains the faster development of the instability in the centre of the layer, in addition to that observed at the very edge, where the interface has a large curvature caused by the contact line.

The development of the instability is monitored either by a video recording or by photographs taken at fixed intervals. The deformation of the interface is revealed by two different techniques. The first one is very simple and consists in strongly dyeing the oil. The intensity of light transmitted through the oil layer decreases exponentially with the thickness of the layer. Then thicker parts appear as darker spots on the photographs (figure 3). This allows us to do a simple determination of the spatial structure of the instability. In the second technique, a ruled screen is photographed through the oil layer (figure 2). The refraction of the light rays on the oil–air interface shifts the apparent position of the lines of the ruled screen. When the slope of the interface remains small, the local apparent displacement of the screen δ is proportional to the local slope of the interface $\alpha = \mathrm{d}\zeta/\mathrm{d}x$:

$$\delta = \alpha(n_0-1)[D+e_g(1-1/n_g)]. \tag{2.4}$$

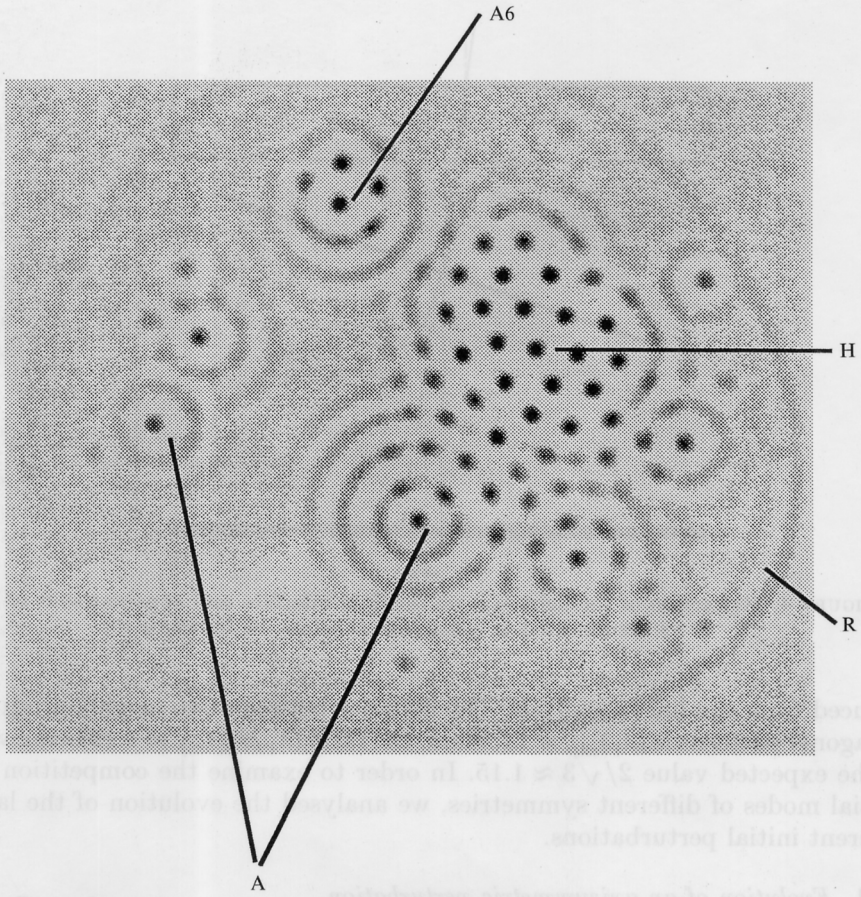

FIGURE 3. Typical structures occurring in the instability. Thicker parts of the fluid layer appear as darker spots. The two structures designated A are initially axisymmetric and were initiated by small dust on the interface. These structures are likely to develop a six-fold symmetry like the one designated A6 and finally evolve into an hexagonal pattern like H. Line structures are also observed. The one shown by R was initiated by the thickness gradient close to the edge of the fluid layer.

where n_0 and n_g are the refraction indices of the oil and glass, e_g is the thickness of the glass plate and D is the distance from the ruled screen to the interface (figure 4). With $D = 56$ mm, $e_g = 5$ mm, $n_0 = 1{,}41$, $n_g = 1{,}52$ and a mesh m of the ruled screen equal to 0.8 mm, a displacement $d = m$ corresponds to a slope of the interface $\alpha = 0.03$. The smallest displacement which can be detected is of the order of magnitude $\frac{1}{5}m$, corresponding to a slope $\alpha = 0.006$.

The image of the screen through an axisymmetric perturbation of the interface is a 'vasarelyan' figure such as the ones shown on figure 5.

2.2. *Experimental results*

As can be seen on figure 3 different patterns can be observed simultaneously in the unstable layer: axisymmetric patterns (concentric rings), axisymmetric patterns whose rings break into peaks (often with a six-fold symmetry), hexagonal patterns and, finally, lines which we sometimes call 'rolls'. The distance between two rolls is $(\lambda_M)_{exp} = 12.5$ mm in rather good agreement with the expected value $\lambda_M = 13.2$ mm

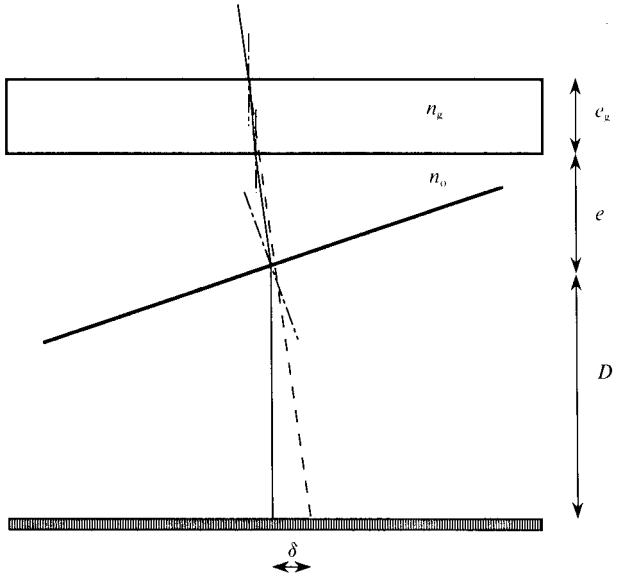

FIGURE 4. Refraction of the light rays on the fluid interface and apparent shift of a ruled screen located at a distance D below the interface.

deduced from the linear analysis. The distance between two neighbouring peaks in hexagonal patterns is $(\lambda_P)_{exp} = 14.9$ mm, the ratio $(\lambda_P/\lambda_M)_{exp} \approx 1.19$ being very close to the expected value $2/\sqrt{3} \approx 1.15$. In order to examine the competition between spatial modes of different symmetries, we analysed the evolution of the layer with different initial perturbations.

2.2.1. *Evolution of an axisymmetric perturbation*

Unless extreme care is taken to protect the oil layer during the long spreading operation, small specks of dust from the ambient atmosphere fall on the interface and create small circular dimples on the free surface (the spatial extent of these perturbations is of order of λ_c (Nicolson 1949; Cloitre 1989)). Very often, the instability of the interface grows from these initial perturbations as concentric rings (figure 3). Meanwhile, clean parts of the oil layer do not show any appreciable deformation during the first half-hour following the overturning of the glass plate. This demonstrates that the development of the instability is very sensitive to the initial amplitude of the deformation.

The time evolution of an isolated axisymmetric pattern is shown on figure 5 as a series of photographs of the deformed ruled screen. From the initial bump in the interface, concentric rings develop outwards and up to four or five rings are frequently seen. From the time evolution of the slope of the interface at a given point, it is possible to give an estimate of the time constant of the instability $\tau_{exp} = 200$ to 300 s, in qualitative agreement with the linear analysis giving $\tau_M = 350$ s.

When the curvature of the interface is too large, the image of the screen through the oil layer disappears (see centre of figure 5*e*). In addition to the sideways displacement of the image, the interface acts as a lens and moves the image out of the depth of field of the viewing optics. This is a typical effect encountered in the use of deflectometry techniques on fluid interfaces (Cloitre 1989).

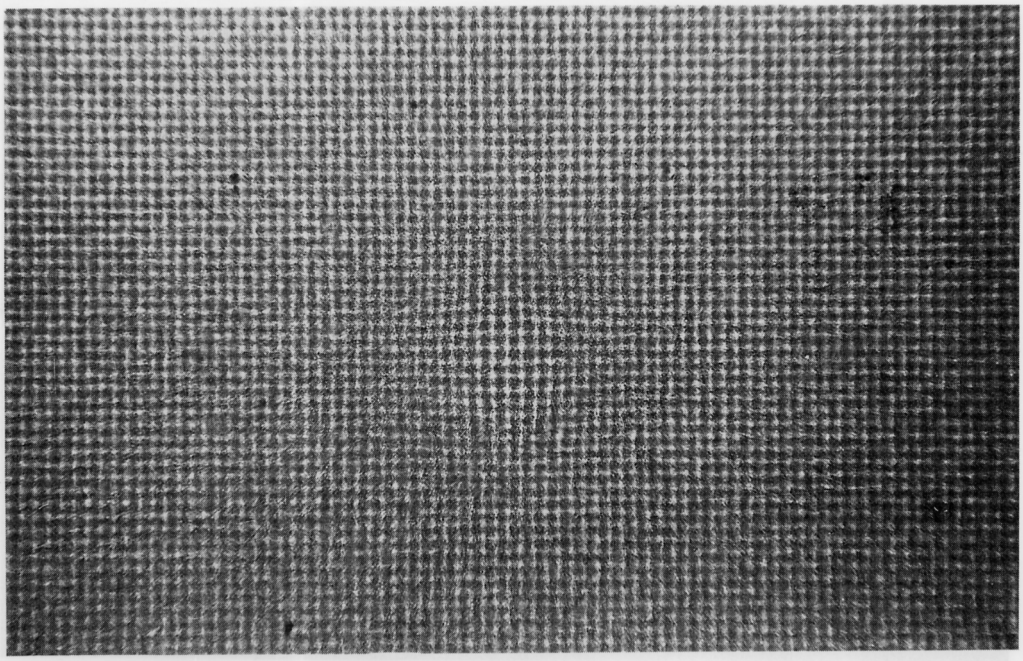

(*a*)

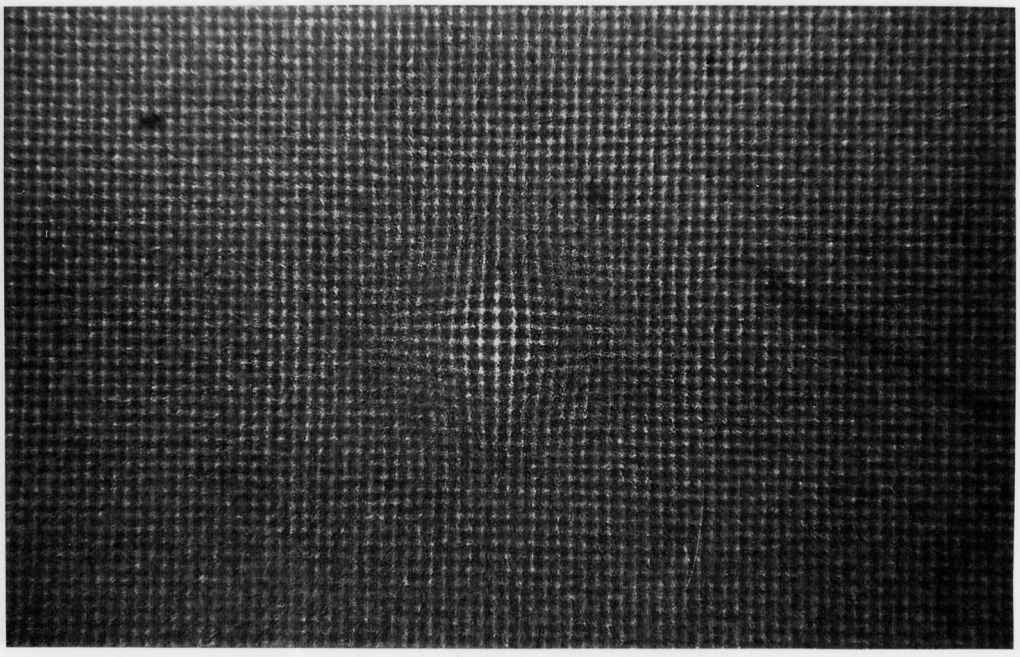

(*b*)

FIGURE 5(*a*, *b*). For caption see page 537.

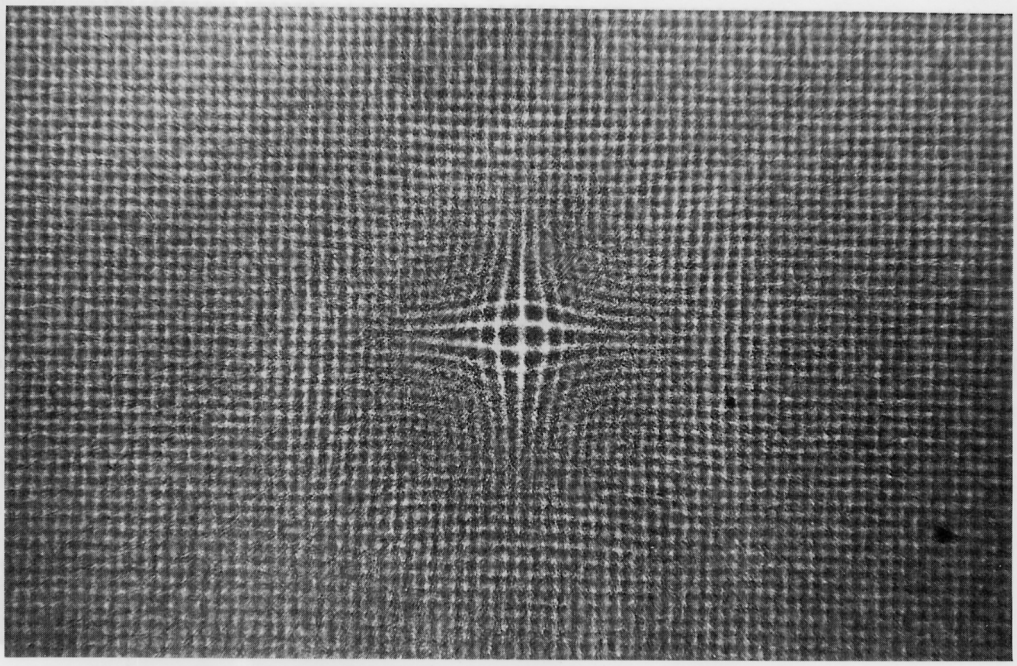

(*c*)

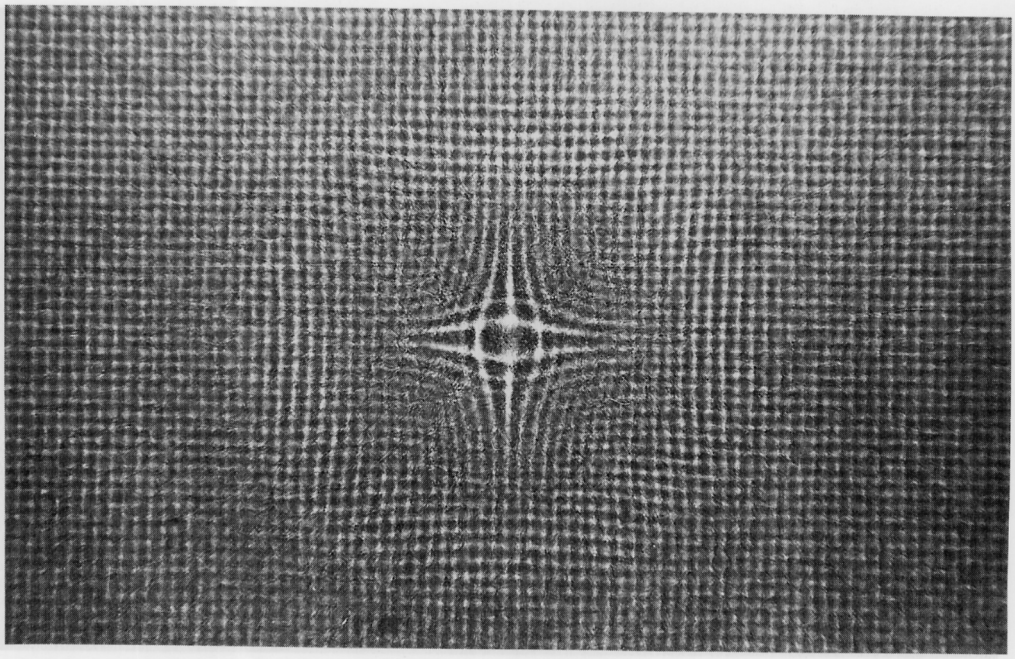

(*d*)

FIGURE 5(*c*, *d*). For caption see facing page.

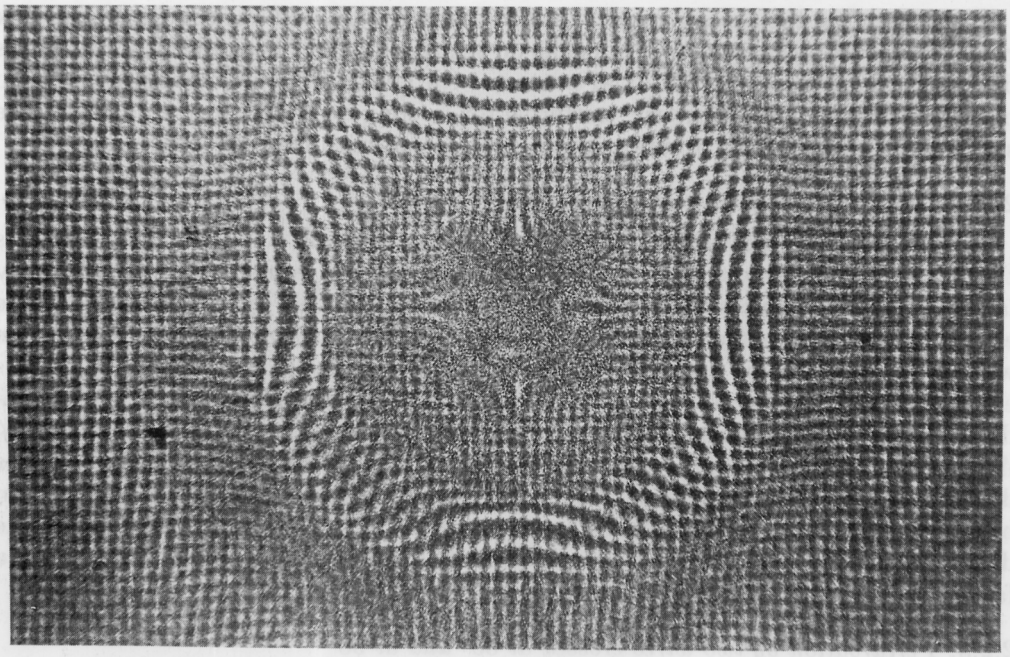

(*e*)

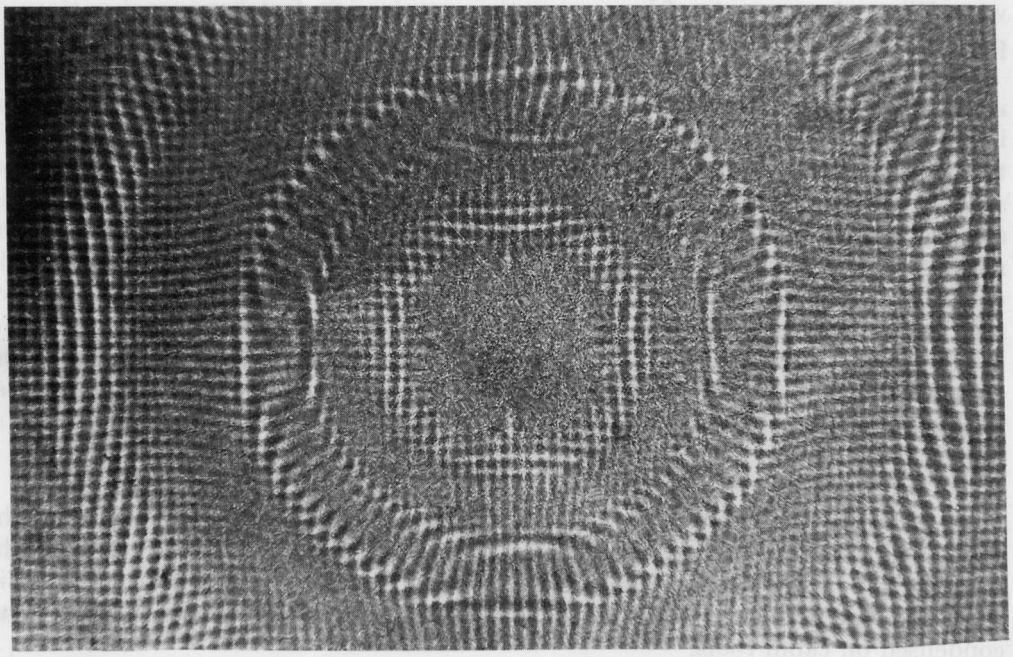

(*f*)

FIGURE 5(*a–f*). Time evolution of an axisymmetric perturbation revealed by the distortion of a ruled screen observed through the interface. The period of the screen is 0.8 mm.

At later times, the axial symmetry is broken into a six-fold one (figure 6), with six peaks on the first ring and twelve peaks on the second ring. Very often, this effect is due to the interaction of the axial pattern with another one. We were not able to observe isolated axisymmetric patterns for a long enough time to test if the symmetry breaking also occurs without interaction with other structures.

2.2.2. *One-dimensional perturbations: lines or 'rolls'*

Additional initial perturbations were made by stretching a thin metal wire across the oil layer after the spreading was completed. The wire has a diameter slightly larger than the thickness of the fluid layer and it is not wetted by the oil. In the stable configuration, before the overturning of the plate, the interface is depressed by the wire. The perturbation is easily calculated from the Laplace equation: it decays exponentially from the wire as $\exp(-|x|\lambda_c)$. Once the glass plate is inverted, one-dimensional structures (lines parallel to the wire) develop from the wire (figure 7). Again, the distance between two neighbouring lines is close to λ_M. These structures do not remain one-dimensional: after a while, the lines are broken into peaks in an hexagonal pattern. The first peaks appear on the wire. Let us mention again that the distance between two peaks along a line parallel to the wire is larger than λ_M by a factor $2/\sqrt{3}$.

2.2.3. *Perturbation by two wires crossed at* 60° *and at* 90°

The tendency of the system to develop a pattern with a triangular symmetry is enhanced if the initial perturbation is created by two wires crossed at 60° (figure 8). As in a the experiment with a single wire, a set of lines moves outwards from each wire. When the two sets of lines cross they create a perfect hexagonal pattern of peaks.

In order to test the stability of a square pattern of peaks (as it is observed, for instance, in the surface instability of ferrofluids with a magnetic field normal to the interface – see Wesfreid & Allais 1985), the experiment was also performed with two wires crossed at 90° (figure 9). At a late stage (figure 9*i*), when the instability has spread all over the fluid pancake, the quadrangular symmetry is observed only in some areas of the fluid. The tendency to go back to the triangular symmetry can be made somewhat quantitative by counting the number of neighbours of each peak, using the skeletonization from image treatment. On figure 9(*i*), 8% of peaks have four neighbours, 32% five neighbours and 60% six neighbours.

The overall conclusion of these experiments is that the preferred symmetries in the gravitational instabilities of thin films are the axial symmetry and the hexagonal symmetry in the initial nonlinear stage.

2.2.4. *Final stage of the experiment: dripping*

At the last stage of the experiment, typically two hours after the start with the conditions given in §2.1, enough fluid has been accumulated in the peaks of the interface for them to become unstable. The fluid then begins to drip from the solid surface, a phenomenon well known to painters and sailors awakened by water condensed on cabin roofs.

Although we did not observe it, there should exist a threshold to this dripping instability. If the initial thickness e_0 is small enough, the volume of fluid accumulated from a surface area of order $\frac{1}{4}\pi\lambda_M^2$ will be too small to exceed the critical volume for the stability of a hanging drop. Myshkis *et al.* (1987) determined the critical volume V^* of an isolated drop as a function of the contact angle of the fluid interface with

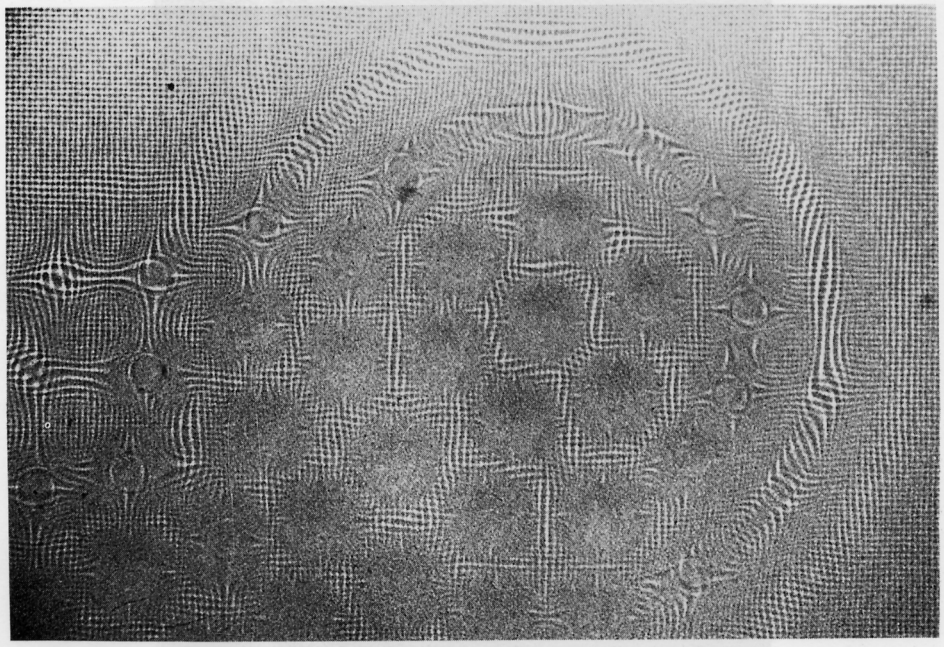

FIGURE 6. Axisymmetric structure of figure 5 at a later stage, when the axial symmetry has been broken.

the solid interface. In our experiment the contact angle is zero (a film of oil always remains on the glass) and $V^* = 19\lambda_c^3$. If the fluid is collected from an hexagon of area $16\pi^2\lambda_c^2/\sqrt{3}$, the critical thickness is given by $e^* = (19\sqrt{3}/16\pi^2)\lambda_c$, and is associated with a critical Bond number $B_c = (e^*/\lambda_c)^2 \approx 0.04$. In our case, its value is 0.31 mm which is larger than the initial thickness in our experiment. According to the above criterion, and contrary to our observations, oil should not drip from the glass plate. The discrepancy probably arises from the fact that the drops are not isolated and are connected to a large reservoir through a tiny film. Very often, dripping occurs after the pairing of two neighbouring peaks which then form a peak large enough to exceed the critical volume V^*. Such pairings can be seen on figures 9*d*, 9*e* and 9*f*, in the upper right-hand corner of the fluid layer. Once it has started, the dripping phenomenon occurs at random positions (and presumably at random times) and destroys the spatial regularity of previously well-organized structures such as the one observed with two wires at 60° (figure 10).

In the one-dimensional case, the existence of a critical Bond number has also been found numerically by Yiantsios & Higgins (1989). The same argument of drop stability allowed them to calculate a value for B_c that was in agreement with their numerical observations. Interestingly, their data also exhibit a tendency towards drop coalescence at the latest stages of the instability for $B < B_c$.

3. Theoretical discussion

3.1. *Evolution equation – linear growth*

The geometry of the experiment is recalled on figure 11. At time $t = 0$, a thin layer of viscous fluid (mass density ρ, viscosity η, thickness e_0) is submitted to a destabilizing gravity field $\boldsymbol{g} = g\boldsymbol{z}$. At time t, the fluctuations of the interface are

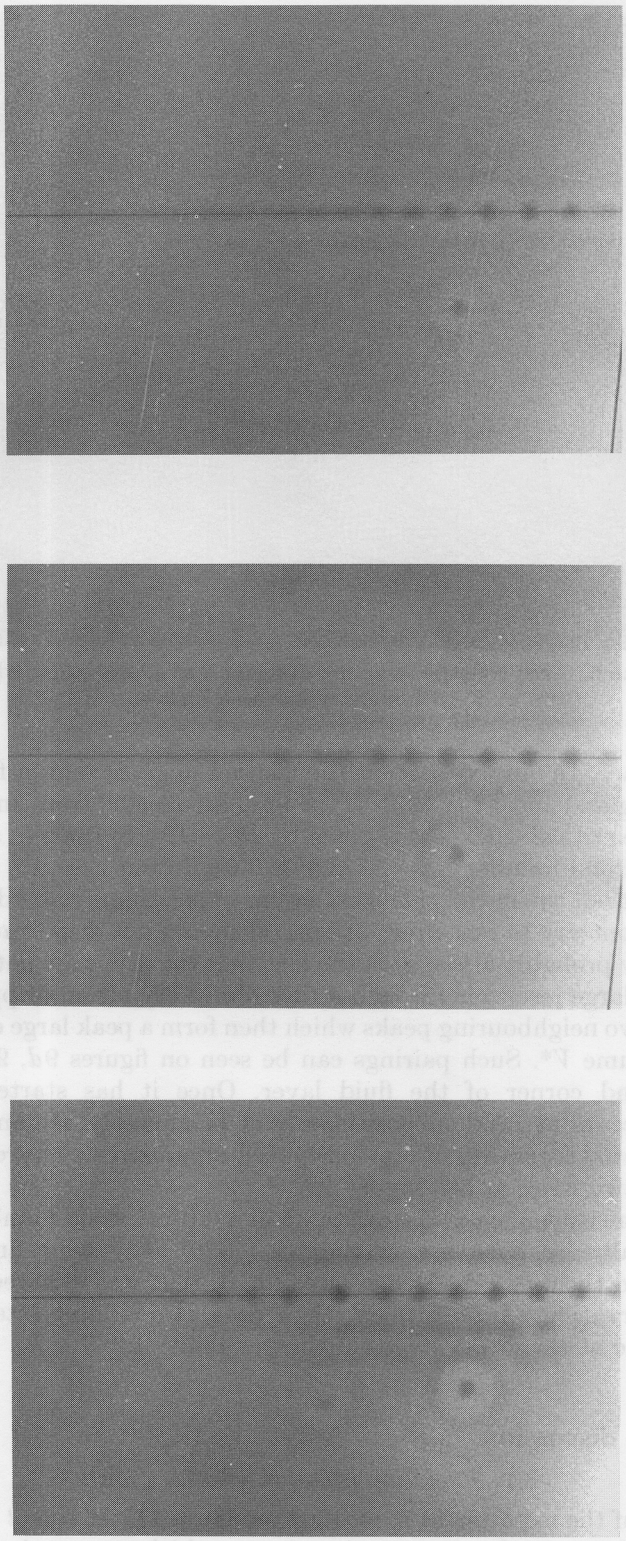

FIGURE 7 (*a–c*). For caption see facing page.

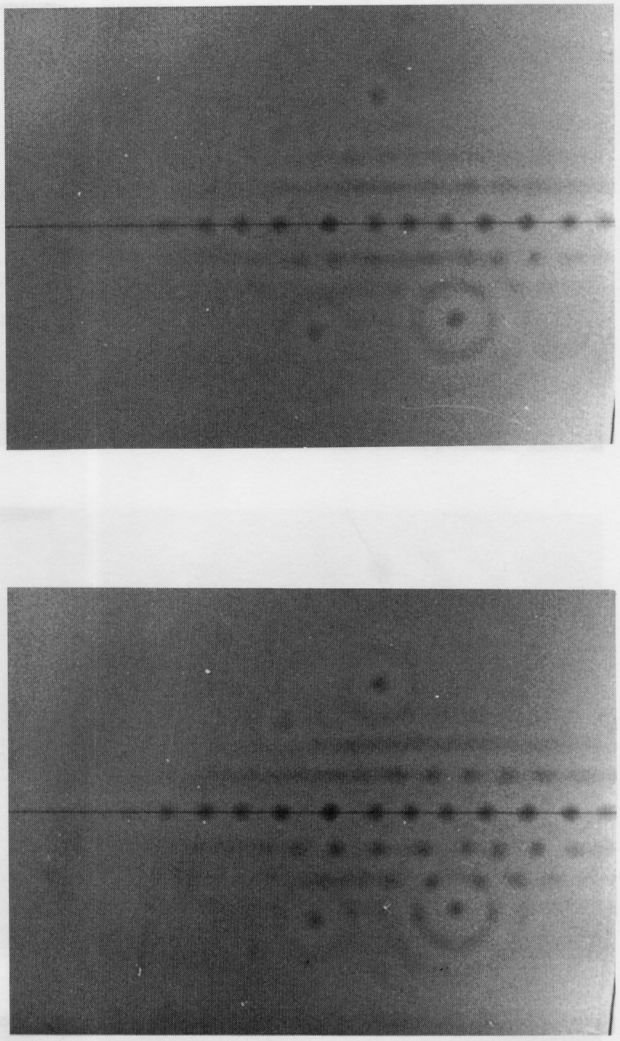

FIGURE 7 (*a–e*). Time evolution of the instability imitiated by a single wire stretched through the fluid layer.

amplified, and the local thickness becomes a function of the position $\boldsymbol{r}$ in the plane (x, y): $e(\boldsymbol{r}, t) = e_0 + \zeta(\boldsymbol{r}, t)$, $\zeta(\boldsymbol{r}, t)$ being the surface displacement. In this section we establish an evolution equation for ζ, which holds in the experimental conditions presented in §2.2. We also specify its general validity conditions after briefly discussing the linear growth regime.

In view of the typical features of our experiment (very long timescales, very viscous fluid, etc.), we neglect the inertial effects. The Navier–Stokes equations reduce in this case to the Stokes ones, and the flow is governed by the following set of equations:

$$\eta \nabla^2 \boldsymbol{u} + \eta\, \partial^2 \boldsymbol{u}/\partial z^2 = \nabla P, \tag{3.1a}$$

$$\eta \nabla^2 v_z + \eta\, \partial^2 v_z/\partial z^2 = \partial P/\partial z - \rho g, \tag{3.1b}$$

$$\nabla \cdot \boldsymbol{u} + \partial v_z/\partial z = 0, \tag{3.1c}$$

where $\boldsymbol{u} = (v_x, v_y)$ and v_z are respectively the horizontal and vertical components of

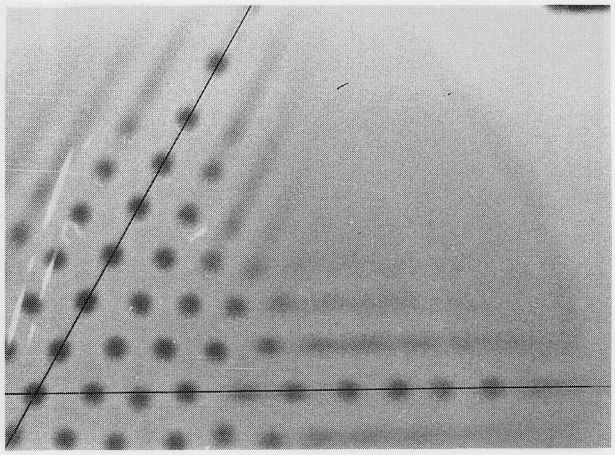

(*a*)

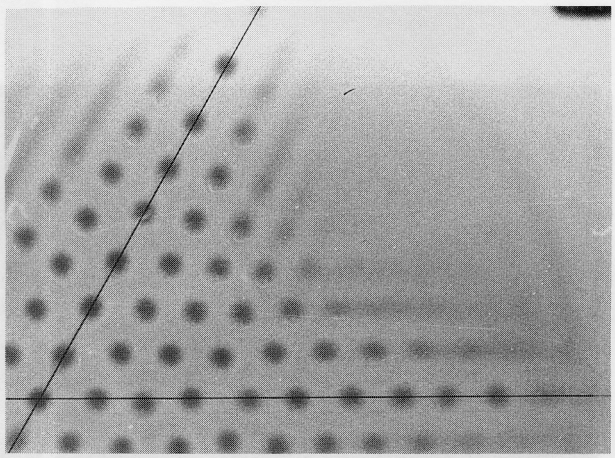

(*b*)

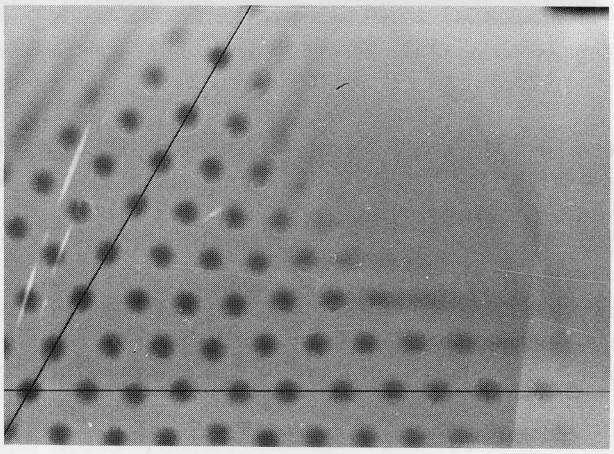

(*c*)

FIGURE 8(*a–c*). For caption see facing page.

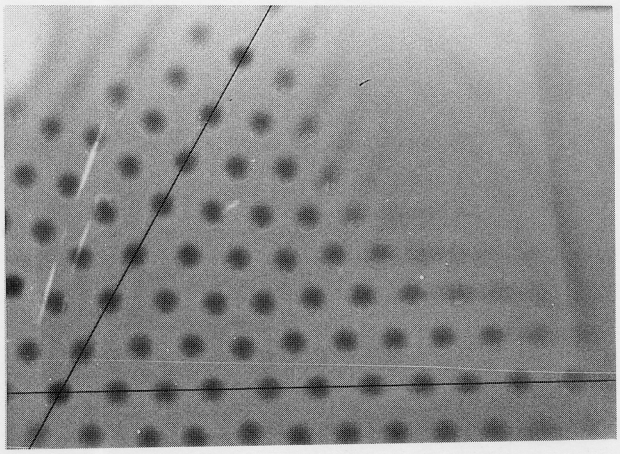

(*d*)

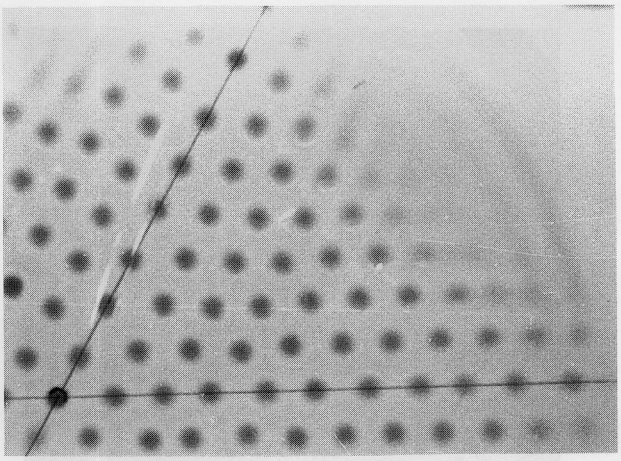

(*e*)

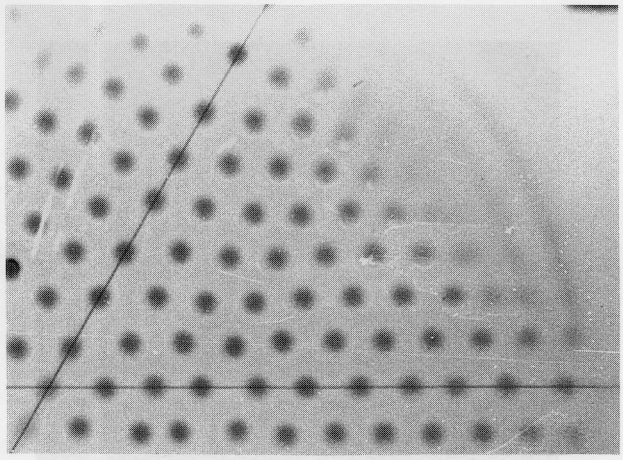

(*f*)

FIGURE 8(*a–f*). Time evolution of the instability initiated by two wires crossed at 60°. The time interval between two pictures is 240 s.

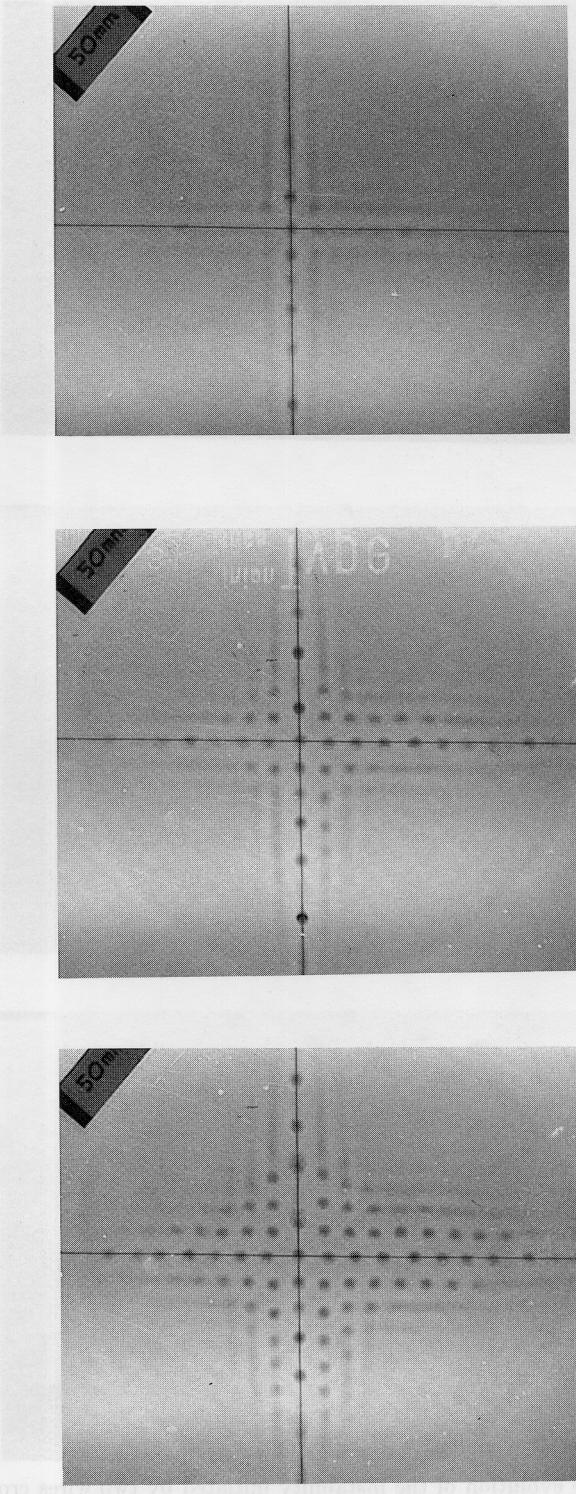

FIGURE 9(*a–c*). For caption see page 366.

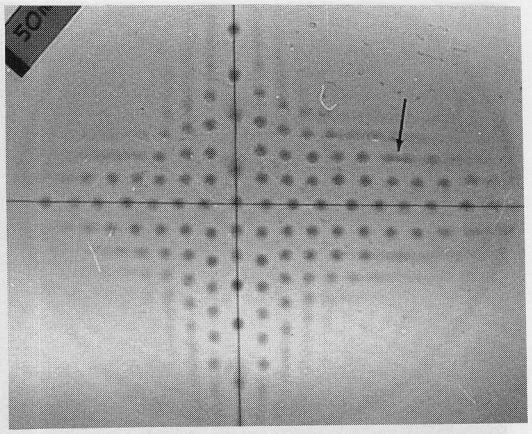

(*d*)

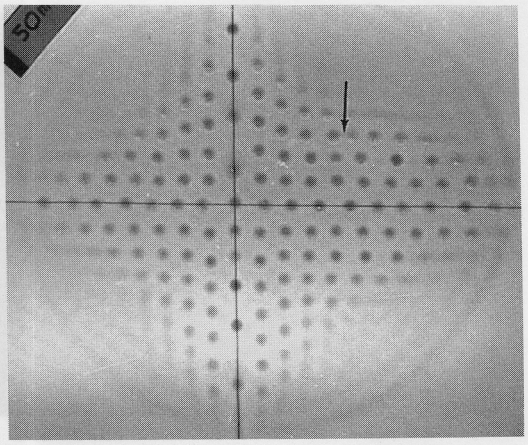

(*e*)

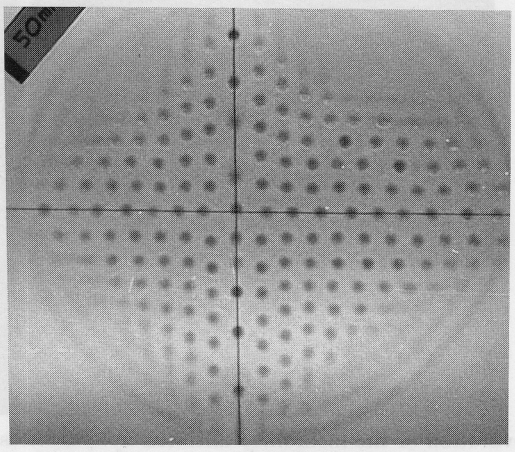

(*f*)

FIGURE 9(*d–f*). For caption see page 366.

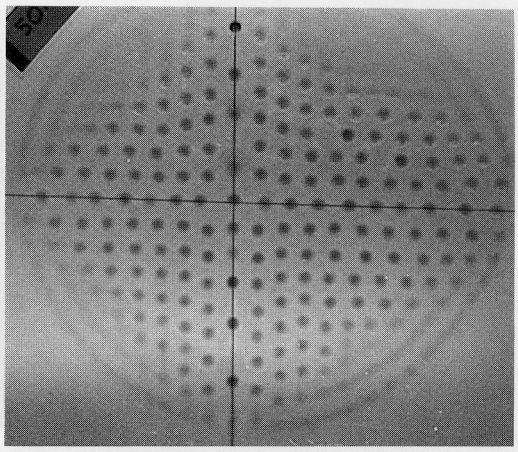

(*g*)

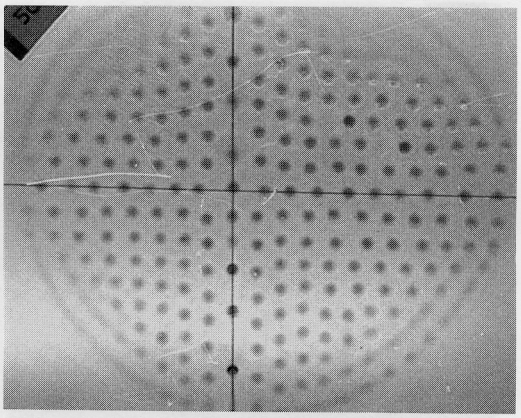

(*h*)

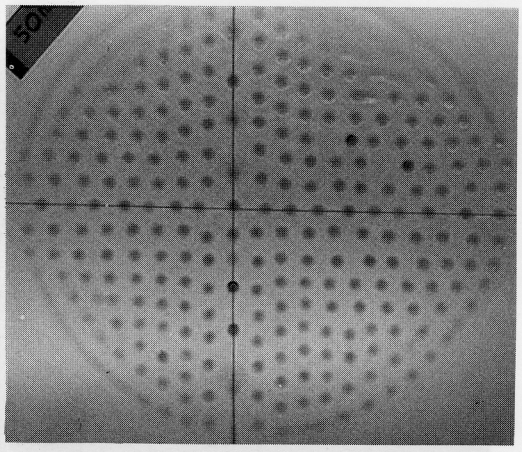

(*i*)

FIGURE 9(*a–i*). Time evolution of the instability initiated by two wires crossed at 90°. The time interval between two pictures is 360 s. Pairing of two neighbouring peaks is indicated by arrows.

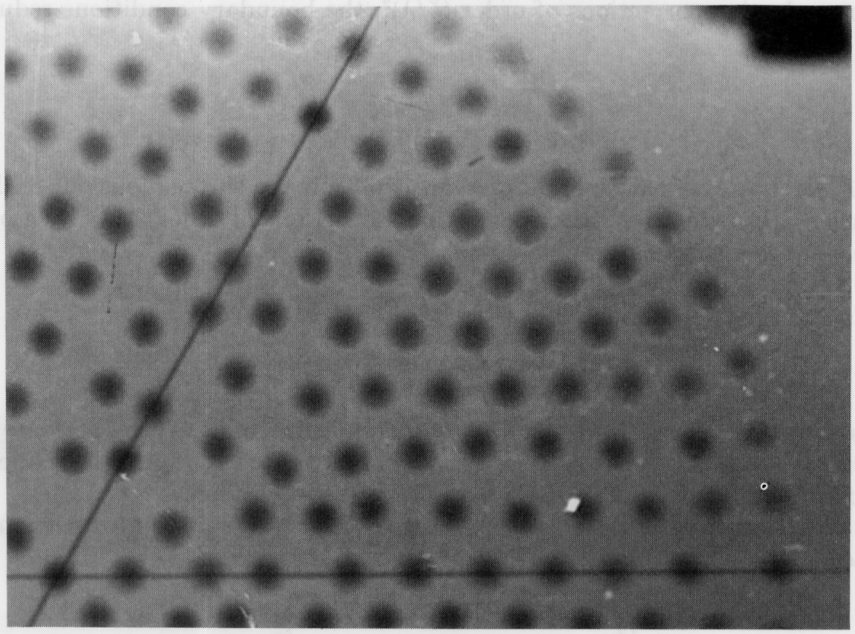

FIGURE 10. Late stage of the hexagonal pattern shown on figure 8. Dripping has already occurred close to the crossing of the wires and begins to disorganize the regular array of peaks.

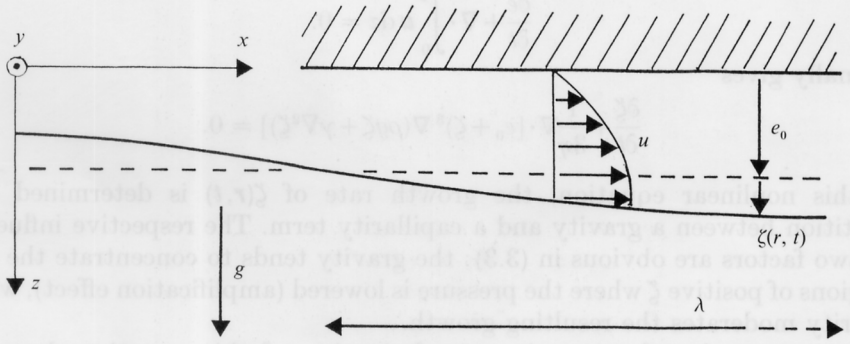

FIGURE 11. Schematic representation of the unstable layer. In the limit $e_0 \ll \lambda_c$, the slope of the interface is negligible, and the velocity field reduces to that of a half-Poiseuille flow.

the velocity and $P(\boldsymbol{r}, z, t)$ is the pressure field. By convention, the gradient operators $\boldsymbol{\nabla}$, and the Laplacian ∇^2 are relative to the x- and y-coordinates throughout.

These equations must be completed by the appropriate boundary conditions. The non-linearities are introduced at this step by the conditions involved at the moving interface. A first study of the problem has been made by Whitehead & Luther (1975) in the limit of a negligible surface tension. In this case, the dominant wavelength of the instability λ_M was comparable to the depth of the layer. In our case, the situation is very different: the layer thickness e always remains very small compared to λ_M, which is in fact determined by the competition between capillarity and gravity. As a result, the slope of the interface remains very small, and the treatment of the problem can be greatly simplified by using the lubrication theory (Batchelor 1967). The evolution obtained will hold in the linear regime $\zeta \ll e_o \ll \lambda_c$, and also in a nonlinear regime defined as $\zeta \approx e_0 \ll \lambda_c$.

After neglecting corrections of order $(\zeta/\lambda)^2$, the boundary conditions reduce to:

$$\boldsymbol{u} = \boldsymbol{0} \quad \text{at} \quad z = 0, \tag{3.2a}$$

$$\eta\, \partial \boldsymbol{u}/\partial z = 0 \quad \text{at} \quad z = e(\boldsymbol{r}, t), \tag{3.2b}$$

$$P_a - P = \gamma \boldsymbol{\nabla} \cdot \{\nabla e/\{1 + (\boldsymbol{\nabla} e)^2\}^{\frac{1}{2}}\} \approx \gamma \boldsymbol{\nabla}^2 e \quad \text{at} \quad z = e(\boldsymbol{r}, t), \tag{3.2c}$$

where P_a denotes the atmospheric pressure, and γ is the surface tension. Still in the lubrication approximation, after neglecting corrections of order $(e/\lambda)^2$, the pressure and velocity fields are easily calculated:

$$P(\boldsymbol{r}, z, t) = P_a - \rho g(e - z) - \gamma \nabla^2 e, \tag{3.3a}$$

$$\boldsymbol{u}(\boldsymbol{r}, z, t) = \frac{1}{2\eta} z(2e - z)\, \boldsymbol{\nabla}(\rho g e + \gamma \nabla^2 e). \tag{3.3b}$$

These approximations lead to a very simple solution of (3.1): the pressure field is hydrostatic, while the horizontal velocity field suggested on figure 11 reduces to a half-Poiseuille flow driven by the horizontal pressure gradient.

The evolution equation can now be deduced from the equation of motion of the interface:

$$\frac{\partial e}{\partial t} + [\boldsymbol{u}_{(z=e)} \cdot \boldsymbol{\nabla}] e = v_{z\,(z=e)} = -\int_0^e \boldsymbol{u}\, \mathrm{d}z,$$

which is equivalent to the mass conservation equation:

$$\frac{\partial e}{\partial t} + \boldsymbol{\nabla} \cdot \int_0^e \boldsymbol{u}\, \mathrm{d}z = 0.$$

This finally gives

$$\frac{\partial \zeta}{\partial t} + \frac{1}{3\eta} \boldsymbol{\nabla} \cdot [e_0 + \zeta)^3\, \boldsymbol{\nabla}(\rho g \zeta + \gamma \nabla^2 \zeta)] = 0. \tag{3.4}$$

In this nonlinear equation, the growth rate of $\zeta(\boldsymbol{r}, t)$ is determined by the competition between a gravity and a capillarity term. The respective influences of these two factors are obvious in (3.3): the gravity tends to concentrate the fluid in the regions of positive ζ where the pressure is lowered (amplification effect), while the capillarity moderates the resulting growth.

A more general and more rigorous derivation of this equation, based on a perturbation expansion, has been recently given by Yiantsios & Higgins (1989) in the case of the two-fluid problem. Equation (3.4) is also mentioned in an article by Pismen (1981), as a special case of the equation describing the flow of a film along an inclined plate, which can be treated with exactly the same methods (Benney 1966; Oron & Rosenau 1989*a*, *b*). We also mention that a one-dimensional version of (3.4) has been found to govern the instability of a thin annular film in a cylindrical capillary (Hammond 1983; Gauglitz & Radke 1988).

We now rewrite (3.4) after separating a linear and a nonlinear contribution:

$$\frac{\partial \zeta}{\partial t} + \frac{e_0^3}{3\eta}(\rho g \nabla^2 \zeta + \gamma \nabla^4 \zeta) + \frac{e_0^2}{3\eta} \boldsymbol{\nabla} \cdot [(3\zeta + 3\zeta^2 + \zeta^3)\, \boldsymbol{\nabla}(\rho g \zeta + \gamma \nabla^2 \zeta)] = 0.$$

The linear operator is classical in the lubrication description of thin films (Vrij 1966; Babchin *et al.* 1983) but, to our knowledge, the properties of the nonlinear part have never been discussed. Most available studies are numerical and restricted to the one-dimensional case (Hammond 1983; Yiantsios & Higgins 1989), or focused on a

different nonlinearity involving terms of the kind $\zeta\partial_x\zeta$ or $(\nabla\zeta)^2$ (Kuramoto 1984; Manneville 1988; Dewel, Borckmans & Walgraef 1984). The term $\zeta\partial_x\zeta$ arises when a mean drift is superimposed on the film flow by means of a shear stress (Babchin *et al.* 1983) or of a component of gravity (Oron & Rosenau 1989*a*, *b*) parallel to the film.

When the perturbation of the interface is small compared to e_0, the nonlinearities can be neglected, and the linear operator leads to an exponential growth of Fourier modes:

$$\zeta_{\boldsymbol{q}}(\boldsymbol{r},t) = \zeta^0_{\boldsymbol{q}}\exp(\mathrm{i}\boldsymbol{q}\cdot\boldsymbol{r})\exp(\sigma_q t),$$

with, just as in (1.3),

$$\sigma_q = (e_0^3/3\eta)(\rho g q^2 - \gamma q^4). \tag{3.6}$$

We thus recover the results announced in §1.3, in particular the selection of a dominant wavenumber q_{M}, given by $q_{\mathrm{M}}^2 = \rho g/2\gamma = 2\pi/\lambda_{\mathrm{M}}$ and associated with a typical growth rate $\sigma_{\mathrm{M}} = e_0^3\rho^2 g^2/12\eta\gamma$. A particular class of solutions is obtained by solving the linear part of (3.5) in polar coordinates (r,θ), giving

$$\zeta_{q,n}(\boldsymbol{r},t) = \zeta^0_{q,n} J_n(qr)\cos[n\theta]\exp(\sigma_q t), \tag{3.7}$$

σ_q being again given by (3.6), and the J_n being the Bessel functions of the first kind. The solution $n = 0$ corresponds to the axisymmetric structures observed in our experiment around the dust. As we will see in §3.5, the annular system with secondary maxima reproduced on figure 6 can be analysed as superpositions of J_0 and J_n patterns, n being multiples of 6.

We now make more precise the validity conditions of (3.4). As usual in lubrication calculations the approximations made on the velocity field are of order α^2, $\alpha \approx \zeta/\lambda_{\mathrm{c}}$ being the typical slope of the interface. Except in the case when dripping occurs, ζ is at most of order e_0 and we obtain a first validity condition:

$$e_0^2/\lambda^2 \approx e_0^2\rho g/\gamma \ll 1. \tag{3.8}$$

We have also checked that the nonlinearities involved at the boundary due to the interface slope were of the same order. The relevant nonlinearities retained in (3.4) are thus only those involved through the vertical displacement of the interface, which modifies the 'mobility' $(e_0+\zeta)^3$ of the fluid in the horizontal pressure gradient.

Another condition is obtained by considering the inertial terms that we have neglected in the Navier–Stokes equations. We have estimated the Reynolds number of the flow calculated above, which reduces to $Re \approx e\zeta/l^2$, l being the viscous diffusion scale given by $l^2 = \eta/\rho\sigma_{\mathrm{M}}$. The second validity condition is thus given by:

$$e_0^2/l^2 \approx e_0^5\rho^3 g^2/\lambda\eta^2 \ll 1. \tag{3.9}$$

A quantity similar to l is involved in the propagation of gravity–capillarity waves on the surface of a viscous fluid (Leblond & Mainardi 1987). In this problem, the spatial extent of the velocity field in the z-direction is determined by the wavelength λ, and also by l. This lengthscale has also been taken into account in recent studies of the magnetic instability of a thin film of ferrofluids spread on the free surface of a heavier liquid (Valet & Wesfreid 1988; Lister & Kerr 1989). In the case of our experiment, $e_0^2/\lambda_{\mathrm{c}}^2$ is of order 10^{-2}, while e_0^2/l^2 is about 10^{-4}. The lubrication model is thus perfectly valid in this case. We should mention another limitation of our approach contained in the nonlinearity of (3.4): at later stage of the instability, harmonics of small wavelength will be excited, and the condition (3.8) will not remain true for these wavelengths. However, our calculations will be limited to the third order growth, that involves only the first harmonics, and this problem will not be relevant here.

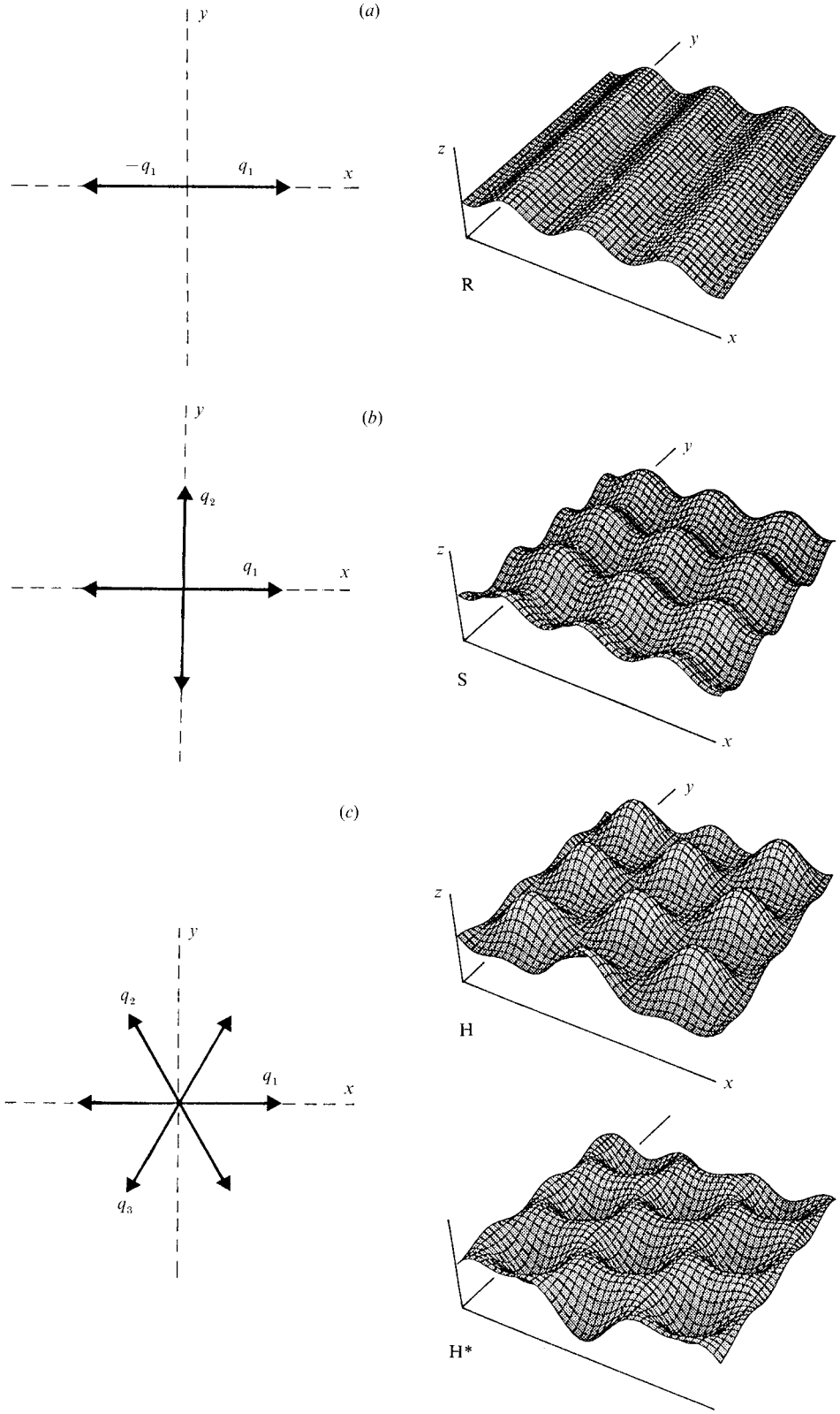

FIGURE 12(*a–c*). For caption see facing page.

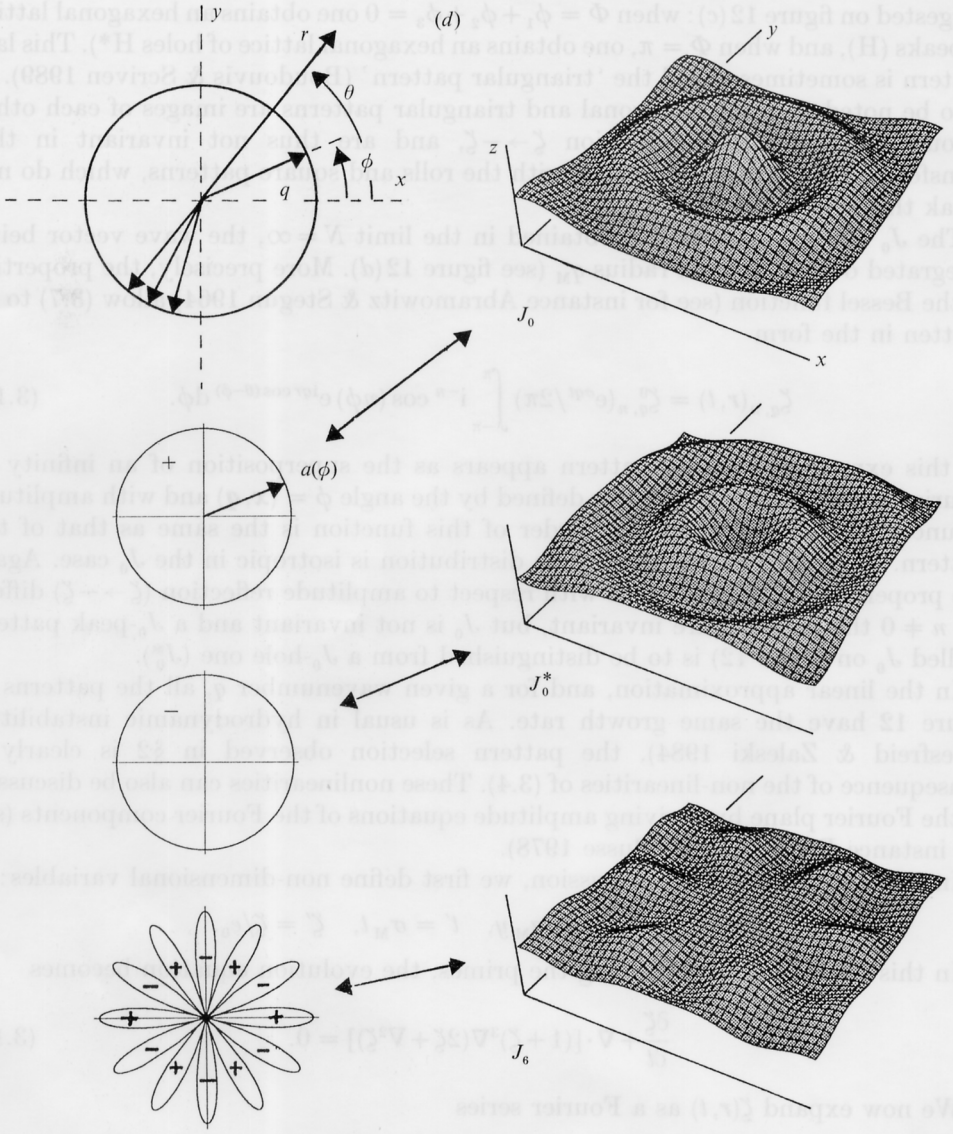

FIGURE 12. The various patterns obtained by superposition of N pairs of modes of equal amplitude. (*a*) 'Roll' system $N = 1$; (*b*) square pattern $N = 2$; (*c*) hexagonal-peak pattern and hexagonal-hole pattern $N = 3$; (*d*) the J_0-peak pattern, the J_0-hole one (J_0^*), and more generally all the J_n patterns, are obtained in the limit $N = \infty$, the wave vector being integrated over a circle. We have also suggested the angular dependence of the amplitude $a(\phi)$.

3.2. *Nonlinear growth of two-dimensional patterns*

The various patterns described in §2 can be viewed as superpositions of N pairs of modes $(\boldsymbol{q}_i, -\boldsymbol{q}_i)$ with $\zeta_{-qi} = \zeta_{qi}^*$ and $\boldsymbol{q}_i = \boldsymbol{q}_M$, to which one should add harmonics in the nonlinear growth. Different possibilities are suggested on figure 12. The 'roll' system (R), the square pattern (S) and the hexagonal one, respectively correspond to $N = 1$, 2, and 3. Because of the translational invariance, the relative phase ϕ_i of the different Fourier modes $\zeta_{qi} = \zeta_{qi} \exp(i\phi_i)$, can be selected without any restriction in the 'rolls' and 'squares' cases. In the case $N = 3$, the nature of the pattern obtained does depend on this choice (Buzano & Golubitzky 1983). Two extreme cases are

suggested on figure 12(*e*): when $\Phi = \phi_1+\phi_2+\phi_3 = 0$ one obtains an hexagonal lattice of peaks (H), and when $\Phi = \pi$, one obtains an hexagonal lattice of holes H*). This last pattern is sometimes called the 'triangular pattern' (Boudouvis & Scriven 1989). It is to be noted that the hexagonal and triangular patterns are images of each other through the amplitude reflection $\zeta \to -\zeta$, and are thus not invariant in this transform. This is to be compared with the rolls and square patterns, which do not break this symmetry.

The J_0 and J_n patterns are obtained in the limit $N = \infty$, the wave vector being integrated over a circle of radius q_M (see figure 12(*d*). More precisely, the properties of the Bessel function (see for instance Abramowitz & Stegun 1964) allow (3.7) to be written in the form

$$\zeta_{q,n}(\boldsymbol{r},t) = \zeta^0_{q,n}(e^{\sigma_M t}/2\pi)\int_{-\pi}^{\pi} \mathrm{i}^{-n}\cos(n\phi)\,e^{\mathrm{i}qx\cos(\theta-\phi)}\,\mathrm{d}\phi. \tag{3.10}$$

In this expression, the J_n pattern appears as the superposition of an infinity of Fourier modes, with wave vector defined by the angle $\phi = (\boldsymbol{x},\boldsymbol{q})$ and with amplitude a function of ϕ. The symmetry order of this function is the same as that of the pattern. In particular, the amplitude distribution is isotropic in the J_0 case. Again the properties of these patterns with respect to amplitude reflection ($\zeta \to -\zeta$) differ: for $n \neq 0$ the patterns are invariant, but J_0 is not invariant and a J_0 peak pattern (called J_0 on figure 12) is to be distinguished from a J_0 hole one (J_0^*).

In the linear approximation, and for a given wavenumber q, all the patterns of figure 12 have the same growth rate. As is usual in hydrodynamic instabilities (Wesfreid & Zaleski 1984), the pattern selection observed in §2 is clearly a consequence of the non-linearities of (3.4). These nonlinearities can also be discussed in the Fourier plane by deriving amplitude equations of the Fourier components (see for instance Palm 1975, or Busse 1978).

In order to simplify this discussion, we first define non dimensional variables:

$$x' = q_M x, \quad y' = q_M y, \quad t' = \sigma_M t, \quad \zeta' = \zeta/e_0.$$

In this notation after dropping the primes, the evolution equation becomes

$$\frac{\partial\zeta}{\partial t} + \boldsymbol{\nabla}\cdot[(1+\zeta)^3\boldsymbol{\nabla}(2\zeta+\nabla^2\zeta)] = 0. \tag{3.11}$$

We now expand $\zeta(\boldsymbol{r},t)$ as a Fourier series

$$\zeta(\boldsymbol{r},t) = \sum_{\boldsymbol{q}} A_{\boldsymbol{q}}(t)\exp(\mathrm{i}\boldsymbol{q}\cdot\boldsymbol{r}).$$

where the $\boldsymbol{q}$ vectors are non-dimensional. The real nature of ζ implies that $A_{-\boldsymbol{q}} = A^*_{\boldsymbol{q}}$, and the mass conservation that $A_0 = 0$. We then develop the cubic term in (3.11) and use the independence of the functions $\exp(\mathrm{i}\boldsymbol{q}\cdot\boldsymbol{r})$. This finally gives

$$\begin{aligned}\frac{\mathrm{d}A_{\boldsymbol{q}}}{\mathrm{d}t} = {} & (2q^2-q^4)A_{\boldsymbol{q}} + 3\sum_{\boldsymbol{q}_a,\boldsymbol{q}_b}(\boldsymbol{q}_a\cdot\boldsymbol{q})(2-q_a^2)A_{\boldsymbol{q}_a}A_{\boldsymbol{q}_b}\delta(\boldsymbol{q}-\boldsymbol{q}_a-\boldsymbol{q}_b) \\ & + 3\sum_{\boldsymbol{q}_a,\boldsymbol{q}_b,\boldsymbol{q}_c}(\boldsymbol{q}_a\cdot\boldsymbol{q})(2-q_a^2)A_{\boldsymbol{q}_a}A_{\boldsymbol{q}_b}A_{\boldsymbol{q}_c}\delta(\boldsymbol{q}-\boldsymbol{q}_a-\boldsymbol{q}_b-\boldsymbol{q}_c) \\ & + \sum_{\boldsymbol{q}_a,\boldsymbol{q}_b,\boldsymbol{q}_c,\boldsymbol{q}_d}(\boldsymbol{q}_a\cdot\boldsymbol{q})(2-q_a^2)A_{\boldsymbol{q}_a}A_{\boldsymbol{q}_b}A_{\boldsymbol{q}_c}A_{\boldsymbol{q}_d}\delta(\boldsymbol{q}-\boldsymbol{q}_a-\boldsymbol{q}_b-\boldsymbol{q}_c-\boldsymbol{q}_d). \end{aligned} \tag{3.12}$$

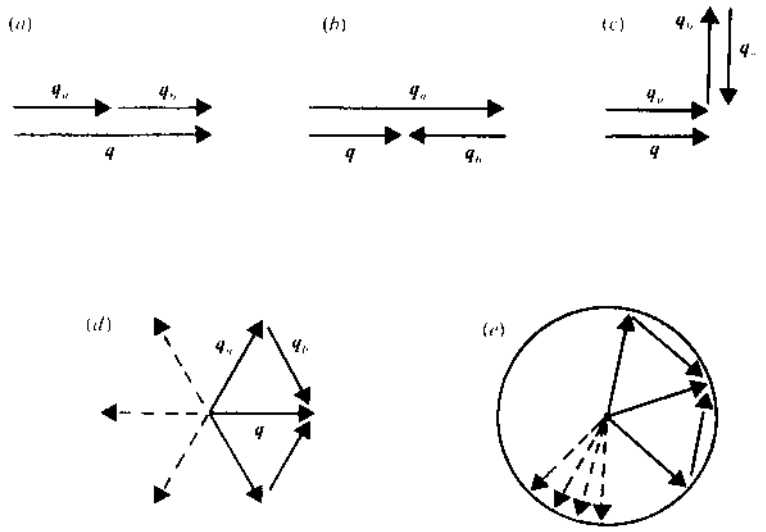

FIGURE 13. Different mode interactions involved in the amplitude equation: (*a*) and (*b*) second order interaction between a main mode and its first harmonic; third-order amplification of a main mode; (*d*) and (*e*) second-order interaction between main modes in the hexagonal and J_0 cases.

The first term on the right-hand side corresponds to the linear growth analysed above, the largest growth rate $\sigma_M = 1$, being obtained for $q = q_M = 1$. The other terms involve selection rules that are suggested on figure 13. All these nonlinear terms can be understood as interactions between triplets, quadruplets and quintuplets of wave vectors. The main peculiarity of (3.12) is the occurrence of a second-order term. This is a very general property of hydrodynamic instabilities that break the symmetry $\zeta \Leftrightarrow -\zeta$ (Buzano & Golubitsky 1983), such as the Bénard–Marangoni one or that of the ferrofluids under a normal field (Cowley & Rosensweig 1967). In our case, this lack of symmetry is obvious in (3.3*b*): changing the sign of ζ not only changes the sign of the fluid velocity but also its magnitude. For this kind of instability, the hexagonal pattern is very often dominant (at least near threshold), and the appearance of this pattern in our experiment is thus not a surprise.

Very often, the discussion of nonlinearities in hydrodynamic instabilities, including the pattern selection problem, is through amplitude equations for the main Fourier modes ($q \approx q_M = 1$), the dynamics of the harmonics being included in the third-order terms. This approach is in fact relevant only in the vicinity of a bifurcation, the distance to the threshold ϵ being treated as a small parameter. This parameter defines in particular the width of the domain of the unstable wave vectors $\Delta q/q_M$ that should scale as ϵ. In our case, there is no such 'control parameter', and the variation of the growth rate in the linear regime depicted on figure 1 corresponds to a ratio $\Delta q/q_M$ of order unity. This situation is reminiscent of the Saffman–Taylor instability. However, the tendency to form an hexagonal pattern can be qualitatively deduced from our equations by defining a new small parameter that is simply the initial amplitude of the perturbations.

If we call ϵ the order of magnitude of the amplitudes of the main modes A_{qi} in the linear regime, the first effect of the nonlinearities will be the generation of harmonics $\boldsymbol{q}_i + \boldsymbol{q}_j$, the amplitude of which will be of order ϵ^2 (figure 13*a*). In turn, these harmonics will interact with the pairs $(\boldsymbol{q}_i, -\boldsymbol{q}_i)$ (figure 13*b*), modifying the growth of the $A\boldsymbol{q}_i$ at order ϵ^3. This correction is to be added to that introduced by the third-

order term of (3.12), which is also of order ϵ^3 (figure 13*c*). Both corrections will be the smallest order ones for the roll and square patterns but not for the hexagonal one. In this case, the relationship $\boldsymbol{q}_1+\boldsymbol{q}_2+\boldsymbol{q}_3=\boldsymbol{0}$ is imposed to take into account the interactions suggested on figure 13(*d*), which introduce a correction of order ϵ^2 in the A_{q_i}. This correction can be studied in the simplest case of three pairs of modes of equal and real amplitudes: $A\boldsymbol{q}_i(t)=A(t)$, for $i=1, 2, 3$. At second order, the harmonics can be neglected and, for $q=q_M=1$, (3.10) reduces to

$$\mathrm{d}A/\mathrm{d}t = A+3A^2. \tag{3.13}$$

We thus obtain that:

(i) the hexagonal pattern of peaks is amplified at order ϵ^2($A>0$);

(ii) the hexagonal pattern of holes is damped at the same order ($A<0$);

(iii) the roll and square patterns are just modified at order ϵ^3, and thus follow linear growth at order ϵ^2.

The results (i) and (ii) also hold for the J_0-peak and the J_0-hole patterns because their Fourier decomposition can be viewed as the superposition of triplets of wave vectors of equal amplitude, the growth of which being governed by (3.11). This remark is illustrated on figures 13(*d*) and 13(*e*), where we see that the same geometrical construction gives the second-order coupling between modes, for the J_0 and hexagonal patterns. At this level of analysis, the hexagonal-peak and J_0 peak pattern appear to be dominant a second order, in agreement with our experimental observations. These observations are related to an important symmetry property of the system studied: the non-invariance under amplitude reflection $\zeta \rightarrow -\zeta$.

Finally, we note that the results (i) and (ii) are consistent with those of Whitehead & Luther (1975) obtained in the limit of vanishing surface tension. Following their calculations, the nonlinearities amplify the growth of hexagonal cells with ascending flow at their centre, and damp the other kind (descending flow). These cells are the equivalent of the hexagonal-peak and hexagonal hole patterns discussed here.

3.3. *Third order growth of rolls, squares and hexagons*

In the case of the rolls, square and hexagonal patterns, we have improved the qualitative arguments developed above by exact calculation at order ϵ^3. The method is similar to that used by Jacobs & Catton (1988*a*, *b*) in the case of the inviscid Rayleigh–Taylor instability. We have considered the growth of an initial disturbance given by $A_{k_i}(0)=\epsilon$ for $i=1$ to N, where the $\boldsymbol{k}_i$ are the main wave vectors suggested on figure 12, and $A_p(0)=0$ for the other wave vectors. When ϵ is a small, positive and real parameter, the cases $N=1$, 2 and 3 correspond to the nonlinear growth of the 'rolls', squares and hexagonal-peak patterns (the hexagonal-hole pattern is obtained for $N=3$ and $\epsilon<0$). We then performed a perturbation analysis by developing the amplitudes as power series in ϵ. For the main modes $\boldsymbol{k}_i$, we have $A_{k_i}(t)=A_k(t)$ with

$$A_k = \epsilon A_{k,1}(t)+\epsilon^2 A_{k,2}(t)+\epsilon^3 A_{k,3}(t)+\dots:$$

for the first harmonics $\boldsymbol{p}=\boldsymbol{k}_i+\boldsymbol{k}_j\neq\boldsymbol{k}_l$, we write

$$A_p = \epsilon^2 A_{p,2}(t)+\epsilon^3 A_{p,3}(t)+\dots:$$

and for the second ones $\boldsymbol{r}=\boldsymbol{k}_i+\boldsymbol{k}_j+\boldsymbol{k}_l\neq\boldsymbol{k}_m$, we would write

$$A_r = \epsilon^3 A_{r,3}(t)+\dots.$$

By identifying the powers of ϵ obtained in (3.12), one obtains a system of equations

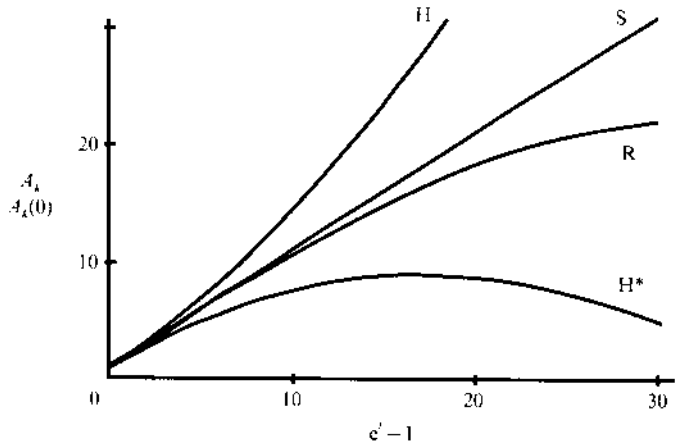

FIGURE 14. Evolution of the amplitudes of the main modes for the roll (R), square (S), hexagonal-peak (H) and hexagonal-hole pattern (H*), calculated at third order for an initial non-dimensional amplitude $A_k = \epsilon = 0.01$. At the precision of the figure, the squared growth cannot be distinguished from the linear one.

in which the order n can be deduced from the orders $n' < n$. The simplest calculations are obtained in the 'roll' case, where by symmetry $A_{k,2} = A_{2k,3} = 0$:

$$\mathrm{d}A_{k,1}/\mathrm{d}t - A_{k,1} = 0, \tag{3.14a}$$

$$\mathrm{d}A_{2k,2}/\mathrm{d}t + 8A_{2k,2} = 6A_{k,1}^2, \tag{3.14b}$$

$$\mathrm{d}A_{k,3}/\mathrm{d}t - A_{k,3} = -15A_{k,1}A_{2k,2} + 3A_{k,1}^3. \tag{3.14c}$$

The solution of this system is easily obtained, giving

$$A_k^{(\mathrm{R})} = \epsilon\,\mathrm{e}^t - 3\epsilon^3[\mathrm{e}^{3t} - \tfrac{11}{8}\mathrm{e}^t + \tfrac{3}{8}\mathrm{e}^{-7t}] + \ldots. \quad A_{2k}^{(\mathrm{R})} = \tfrac{3}{5}\epsilon^2[\mathrm{e}^{2t} - \mathrm{e}^{-8t}] + \ldots. \tag{3.15}$$

where the superscript (R) stands for 'rolls'. We have also carried the same calculation for the square and hexagonal cases. The only difference is that, in addition to the main modes $\boldsymbol{k}_i$ of amplitude A_k, and to the harmonics $2\boldsymbol{k}_i$ of amplitude A_{2k}, a new group of harmonics $\boldsymbol{p}$ of the kind $\pm\boldsymbol{k}_1 \pm \boldsymbol{k}_2$ is to be taken into account, of amplitude $A_{k,k}$. In the square case, we obtain

$$\left.\begin{aligned} A_k^{(\mathrm{S})} &= \epsilon\,\mathrm{e}^t + \tfrac{9}{8}\epsilon^3(\mathrm{e}^t - \mathrm{e}^{-7t}) + \ldots, \\ A_{2k}^{(\mathrm{S})} &= \tfrac{3}{5}\epsilon^2(\mathrm{e}^{2t} - \mathrm{e}^{-8t}) + \ldots. \\ A_{k-k}^{(\mathrm{S})} &= 3\epsilon^2(\mathrm{e}^{2t} - 1) + \ldots. \end{aligned}\right\} \tag{3.16}$$

and in the hexagonal case

$$\left.\begin{aligned} A_k^{(\mathrm{H})} &= \epsilon\,\mathrm{e}^t + 3\epsilon^2(\mathrm{e}^{2t} - \mathrm{e}^t) + \tfrac{1}{5}\epsilon^3[6\,\mathrm{e}^{3t} - 96\,\mathrm{e}^{2t} + \tfrac{1620}{8}\mathrm{e}^t - \tfrac{108}{3}\mathrm{e}^{-2t} - \tfrac{45}{8}\mathrm{e}^{-7t}] + \ldots, \\ A_{2k}^{(\mathrm{H})} &= \tfrac{3}{5}\epsilon^2(\mathrm{e}^{2t} - \mathrm{e}^{-8t}) + \ldots. \quad A_{k+k}^{(\mathrm{H})} = \tfrac{9}{5}\epsilon^2(\mathrm{e}^{2t} - \mathrm{e}^{-3t}) + \ldots. \end{aligned}\right\} \tag{3.17}$$

In figure 14, we have plotted the variation of $A_k(t)/A_k(0)$ for the four patterns: rolls, squares, hexagonal-peaks and hexagonal-holes. These calculations are in perfect agreement with the qualitative analysis developed above and with the experimental results. In particular, we recover that the hexagonal-peak pattern is the dominant one because of the second-order nonlinearities. These nonlinearities tend to damp the hexagonal-hole pattern, which is thus practically impossible to observe.

For the four patterns, the third-order term involves a competition between a third-order amplification and the moderating effect of the harmonics. This appears for instance in (3.14*c*), which holds for the role case. In this case, the harmonics seem to dominate, which is reminiscent of the situation encountered for saturating instability near a supercritical bifurcation. The situation is different in the case of the hexagonal pattern: the third-order term is positive and increases again the growth of this pattern. In the square case, the two effects practically compensate each other, the behaviour obtained being close to the linear one. As a result, the growth rate of the square pattern is intermediate between the rolls and hexagonal-peak ones. This remark is perhaps related to the persistency of the square pattern observed locally in the case of the two wires at 90°.

We finally note that the growth of the first harmonics introduces a modification of the shape of the interface at order ϵ^2. This contribution tends to amplify the peaks and to fill the valleys, increasing the asymmetry of the profile with respect to the plane $z = e_0$. This very general effect is observed in the case of a system that is not invariant under amplitude reflection, such as for instance a ferrofluid interface under a normal field. In our case, this asymmetry has its origin in the difference of the fluid mobility $(e_0+\zeta)^3$ between regions of positive and negative ζ.

3.4. *Rolls hexagon transition*

The comparison of the growth rates of the different patterns made in the previous section allows us to understand qualitatively the reason why some particular symmetries are selected. However, it is clear from figure 14 that the differences between the calculated growth laws are not very pronounced. In addition, and as mentioned above, the growth of the square and roll patterns as well as that of the hexagonal pattern, involves modifications of the interface at order ϵ^2 associated with the amplitudes of the first harmonics $A_{2k}(t)$ and $A_{k,k}(t)$. Strictly speaking, the hexagonal pattern is thus not the only one to be amplified at order ϵ^2. These considerations suggest that a more careful analysis is required to understand the results of the one-wire experiment discussed in §2.2.2.

In this section we show that the selection of the hexagonal pattern does not only result from its larger growth rate. In fact the hexagonal growth can inhibit that of another pattern. This is what happens in the one-wire experiment, that we model as follows. We again consider three pairs of modes such as those suggested on figure 12(*c*), but with different initial amplitudes: $A_{k1}(0) = \epsilon_1$ and $A_{k2}(0) = A_{k3}(0) = \epsilon_2$, where ϵ_1 and ϵ_2 are small, real and positive values. When $\epsilon_2 < \epsilon_1$, this distribution can be viewed as the superposition of a roll system of amplitude $A_R(0) = A_{k1}(0) - A_{k2}(0) = \epsilon_1 - \epsilon_2$, and of an hexagonal perturbation of amplitude $A_H(0) = A_{k2}(0) = \epsilon_2$. In a calculation at second order, we can neglect the influence of the harmonics. In this case, the amplitude equations reduce to

$$\frac{dA_{k1}}{dt} = A_{k1} + 3A^*_{k2}A^*_{k3}, \quad \frac{dA_{k2}}{dt} = A_{k2} + 3A^*_{k1}A^*_{k3}, \quad \frac{dA_{k3}}{dt} = A_{k3} + 3A^*_{k2}A^*_{k1}. \tag{3.18}$$

This system of equations generalizes (3.9) to the case of three modes of different amplitudes. Knowing the initial conditions, the three amplitudes can be treated as real numbers, and (3.18) can be rewritten in terms of amplitudes of the roll and hexagonal pattern components $A_R = A_{k1} - A_{k2}$ and $A_H = A_{k2} = A_{k3}$:

$$\frac{dA_R}{dt} = A_R - 3A_R A_H, \quad \frac{dA_H}{dt} = A_H + 3A_H^2 + 3A_H A_R. \tag{3.19}$$

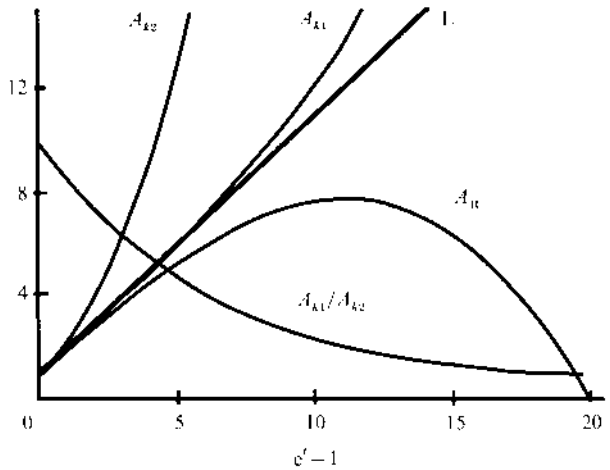

FIGURE 15. Evolution of the reduced amplitudes $A/A(0)$ in the roll–hexagon transition, calculated at second order for $A_{k1}(0) = \epsilon_1 = 0.05$ *and* $A_{k2}(0) = \epsilon_2 = 0.005$. *L* designates linear growth. The long-time behaviour is in fact unphysical, but the tendency toward the hexagonal situation ($A_{k1}/A_{k2} \to 1$) *and the damping of the roll component* (A_R) is well recovered.

A short-time perturbation expansion similar to that used in the previous section gives at order ϵ^2

$$A_R(t) = \epsilon_R\, e^t - 3\epsilon_R\epsilon_H|e^{2t} - e^t|, \quad A_H(t) = \epsilon_H\, e^t + 3\epsilon_H(\epsilon_H + \epsilon_R)|e^{2t} - e^t|. \tag{3.20}$$

On both systems of equations (3.19) and (3.20), we observe that in addition to the nonlinear terms discussed in the previous section, the second-order nonlinearities introduce a coupling between A_H and A_R. This effect tends to damp the growth of the rolls and to increase that of the hexagonal pattern. The hexagonal-peak pattern dominates the roll one not only because of its larger growth rate but also because of the nonlinear interaction between these two patterns at second order.

We also mention that (3.18) can be solved exactly by selecting new variables u_i defined as $A_{qi} = u_i(t)\, e^t$, and by noting that $u_2 = u_3$ and that $u_1^2 - u_2^2$ is constant. After some calculations we obtain

$$A_{k2} - A_H = \frac{(\epsilon_1^2 - \epsilon_2^2)^{\frac{1}{2}} e^t}{\sinh(\phi_s - \phi)}, \quad A_{k1} = \frac{(\epsilon_1^2 - \epsilon_2^2)^{\frac{1}{2}} e^t}{\tanh(\phi_s - \phi)}. \tag{3.21}$$

the quantities ϕ and ϕ_s being defined as

$$\phi = 3(\epsilon_1^2 - \epsilon_2^2)^{\frac{1}{2}}|e^t - 1|, \quad \cosh(\phi_s) = \epsilon_1/\epsilon_2.$$

The evolution of A_{k1} and A_{k2} is suggested on figure 15. We find an unphysical divergence at a finite time t_s given by $\phi(t_s) = \phi_s$, because our calculation is in fact correct only at second order. Of course, at long time, nonlinearities of higher order will modify the growth and presumably remove the singularity. Because of this peculiarity, this solution is not of great practical interest. However, it gives interesting results concerning the behaviour of the ratio A_{k1}/A_{k2}, and of that of the roll amplitude $A_R = A_{k1} - A_{k2}$:

$$A_{k1}/A_{k2} = \cosh(\phi_s - \phi), \quad A_R = (\epsilon_1^2 - \epsilon_2^2)^{\frac{1}{2}} e^t|\cosh(\phi_s - \phi) - 1|/\sinh(\phi_s - \phi).$$

As suggested on figure 15, when t approaches t_y, the ratio A_{k1}/A_{k2} tends toward 1. This means that the perturbed roll pattern evolves toward an hexagonal one, in agreement with the experimental observations. Simultaneously, the roll component of the pattern A_R vanishes at t_y. This result is very important and means that the growth of the hexagonal pattern would lead finally to the complete disappearance of the roll component, just as observed in the experiments. Of course, the correct description of this evolution would require taking into account higher-order nonlinearities, and thus higher order harmonics.

A similar calculation can be developed in the case of the two wires at 60°, but now with $\epsilon_1 \ll \epsilon_2$ Similar results are obtained in this case: the system evolves toward the hexagonal pattern, the two systems of rolls being progressively erased by the hexagonal growth. A more general situation can be studied using (3.20), that is the case of three different, complex, initial amplitudes $A_{ki}(0) = \alpha_i \exp(i\phi_i^0)$ with $\alpha_i > 0$. In all cases the hexagonal-peak pattern is obtained when t approaches t_y. In particular, the ratios α_i/α_j tend towards 1, and the sum of the phases $\Phi = \phi_1 + \phi_2 + \phi_3$ towards 0 (or $2n\pi$). An exception is the case of the hexagonal-hole pattern, for which Φ remains constant and equal to π. It is, however, possible to show that this solution is unstable with respect to Φ variations and finally relaxes toward the hexagonal peak solution.

All these results obtained here at second order are in fact well known, but in a slightly different context. In the case of a two-dimensional instability driven by a control parameter, and close to a bifurcation point, (3.18) is replaced by generalized Landau equations (Haken 1975):

$$\left.\begin{aligned}
\frac{dA_{k1}}{dt} &= \epsilon A_{k1} + f A_{k2}^* A_{k3}^* - g|A_{k1}|^2 A_{k1} - g'A_{k1}(|A_{k2}|^2 + |A_{k3}|^2),\\
\frac{dA_{k2}}{dt} &= \epsilon A_{k2} + f A_{k1}^* A_{k3}^* - g|A_{k2}|^2 A_{k2} - g'A_{k2}(|A_{k1}|^2 + |A_{k3}|^2),\\
\frac{dA_{k3}}{dt} &= \epsilon A_{k3} + f A_{k1}^* A_{k2}^* - g|A_{k3}|^2 A_{k3} - g'A_{k1}(|A_{k2}|^2 + |A_{k2}|^2).
\end{aligned}\right\} \tag{3.22}$$

where ϵ is proportional to the distance to the threshold, and where the precise values of f, g and g' depend on the nature of the nonlinearities. When $f > 0$, and in a wide range of the other parameters, the hexagonal-peak solution is an attractor point, and the hexagonal-hole pattern is an unstable fixed point. In contrast to our second-order truncation, (3.22) leads to a finite amplitude A_H at large times. Unfortunately, and as explained in the previous section this approach is correct only near the bifurcation point $\epsilon = 0$, where the dynamics of the harmonics can be neglected, their influence being reduced to contributions to the third-order terms. In our case this approximation is not justified, and the influence of the third- and fourth-order nonlinearities on the roll–hexagon transition remains to be studied.

3.5. *Simplified study of annular patterns*

We now briefly discuss the case of the annular patterns observed around the dust in §2. Usually, the study of this kind of pattern requires expansion of the interface perturbations over the Bessel functions and deriving new amplitude equations (Normand 1984; Jacobs & Catton 1988*a*, *b*). Unfortunately, the properties of the Bessel functions complicate the calculations, the selection rules disappearing from

the amplitude equations. In this section we propose a simplified approach based on the decomposition of the J_n patterns over the Fourier modes presented in §3.2. We thus consider the evolution of a continuous one-parameter distribution of modes:

$$\zeta(\boldsymbol{r},t)=\int_{\pi}^{\pi} a(\phi,t)\,\mathrm{e}^{\mathrm{i}kr\cos(\theta-\phi)}\,\mathrm{d}\phi, \tag{3.23}$$

with $a(\phi+\pi,t)=a^*(\phi,t)$. Just as in the previous section we will restrict our study to the dominant wavenumber $k=k_M=1$, and to the nonlinearities of second order. As we have seen on figure 13(*e*), the second order coupling between modes is basically the same as that given by (3.20). The evolution equation of $a(\phi,t)$ is thus given by

$$\frac{\partial}{\partial t}a(\phi,t)=a(\phi,t)+3a^*(\phi+\tfrac{2}{3}\pi,t)\,a^*(\phi-\tfrac{2}{3}\pi,t). \tag{3.24}$$

The simplest solution of this equation is obtained for the J_0 patterns. In this case, the amplitude does not depend on ϕ and one obtains, at short times,

$$a(\phi,t)\approx a(0)\,\mathrm{e}+3a(0)^2(\mathrm{e}^{2t}-\mathrm{e}^t),$$

which is identical to the second-order growth law of the hexagonal pattern (see (3.17)). We thus recover that, as announced in §3.2, the J_0 and hexagonal patterns have the same growth law, the J_0-peak and the hexagonal-peak ones being amplified at second order.

If one starts now from a perturbed J_0 pattern, or from another J_n pattern with $n\neq 0$, the ϕ-dependence is to be taken into account. We can, however, simplify the discussion by noting that, in (3.24), the evolution of $a(\phi,t)$ appears as the superposition of those of an infinity of hexagonal patterns, of different orientations, and without interactions. Each of these patterns is defined by six wave vectors: $\pm\boldsymbol{k}(\phi)$, $\pm\boldsymbol{k}(\phi+\frac{2}{3}\pi)$, $\pm\boldsymbol{k}(\phi-\frac{2}{3}\pi)$. We can thus use the results suggested at the end of the previous section: each sub-pattern should evolve toward the hexagonal-peak one. The patterns obtained asymptotically (as second order) must satisfy the following relationships:

$$|a(\phi)/a(\phi+\tfrac{2}{3}\pi)|=1,$$

$$\mathrm{Arg}\,[a(\phi)]+\mathrm{Arg}\,[a(\phi+\tfrac{2}{3}\pi)]+\mathrm{Arg}\,[a(\phi-\tfrac{2}{3}\pi)]=0\quad(\text{modulo }2\pi).$$

It is easy to check that these conditions are satisfied for patterns of the kind

$$\zeta(\boldsymbol{r},t)=\alpha_0(t)\,J_0(r)+\sum_{m\neq 0}\alpha_m(t)\,J_{6m}(r)\cos(6m\theta), \tag{3.25}$$

with $\alpha_0+\sum_{m\neq 0}(-1)^m\alpha_m>0$. This condition prevents sign changes in $a(\phi,t)$ and thus allows the phase condition to be satisfied. The evolution of the α_i is in general very complicated, unless one starts at $t=0$ from a pattern of this kind. In this case the $\alpha_i(t)$ can be deduced from the amplitude evolution that reduces to

$$a(\phi,t)=a(\phi,0)\,\mathrm{e}^t+3a(\phi,0)^2(\mathrm{e}^{2t}-\mathrm{e}^t). \tag{3.26}$$

It is then easy to check that this kind of pattern is also amplified at second order, with a slight evolution of its shape. We thus obtain that, in addition to the axisymmetric and hexagonal structures, another kind of favoured pattern can be obtained by superposition of J_0, J_6 and J_{12} solutions of the linear problem (and more generally J_{6n} solutions). We believe that the structure reproduced in figure 6 is of this kind. This figure can be compared with figure 16 where we have reproduced two

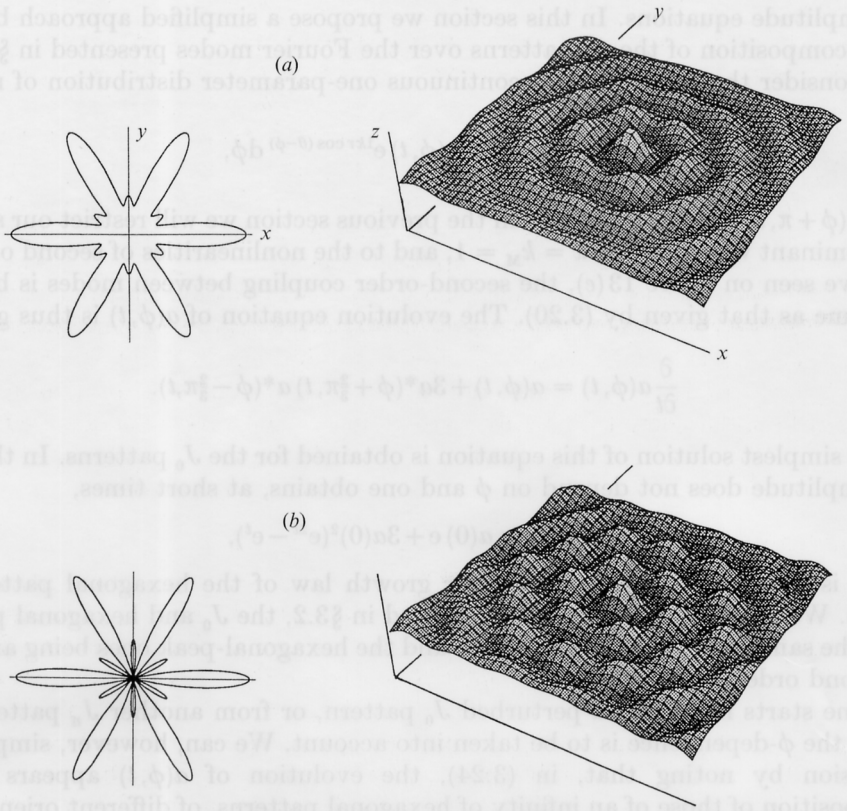

FIGURE 16. Two examples of annular patterns with secondary maxima amplified by the second-order nonlinearities. Both patterns are superposition of J_0, J_6 and J_{12} ones with respective weights α_0, α_1 and α_2. (*a*) $\alpha_0 = 0.75$, $\alpha_1 = 0.5$. $\alpha_2 = 0.25$; (*b*) $\alpha_0 = \alpha_1 = \alpha_2 = 1$. The respective angular dependance $a(\phi)$ of the amplitude is also reproduced.

examples of patterns deduced from equation (3.25). The central maximum is that of the J_0 function, the six secondary peaks on the first ring correspond to $J_0(\mathrm{r})\cos(6\theta)$, and the twelve others on the second ring are associated with the $J_{12}(\mathrm{r})\cos(12\theta)$ component. Depending on the respective weight of the J_n functions, the structure obtained can be very close to a localized hexagonal pattern.

In §2.2.1, we have mentioned that these structures are very often intermediate steps of a transition between the axisymmetric and hexagonal symmetries, initiated by the perturbation of a J_0 structure by another pattern. A precise theoretical and experimental study of this transition remains to be made. We can, however, propose the following qualitative mechanism. Such a transition could be initiated by the interaction between a J_0 pattern and a Fourier component of another pattern. If we identify the Ox axis with the direction of this wave vector, the second-order nonlinearities will contaminate the directions $\phi = \pm\frac{1}{3}\pi$ and $\pm\frac{2}{3}\pi$, leading thus to a pattern of six-fold symmetry of the kind described above. At a later stage, this pattern could evolve towards an hexagonal extended pattern, but the description of this evolution is not possible using our simplified approach.

It is important to realize that the dynamics of the transition between the axial and hexagonal symmetry is presumably very different from that of the roll–hexagon transition. In the first case ($J_0-\mathrm{H}$), both symmetries are amplified at second order, while in the second one ($\mathrm{R}-\mathrm{H}$), only the hexagonal pattern is amplified. Qualitatively,

we expect a greater stability for the axial symmetry than for the 'roll' one. This prediction is in agreement with our experimental observations (compare figures 5 and 7).

Finally, we note that the solutions (3.25) are not invariant under amplitude reflection $\zeta \rightarrow -\zeta$, because of the their J_0 component. These solutions share this property with the hexagonal pattern and of course with the J_0 one. Our system constitutes a very simple example of the influence of the symmetries on hydrodynamic instabilities (see for instance Busse 1978; Buzano & Golubitzky 1983): positive and negative displacements of the interface are not equivalent, a property that leads to the appearance of asymmetrical patterns with respect to the unperturbed interface. In addition, for this kind of instability, the relevant nonlinearities are of second order and favour the interactions of Fourier modes separated by 60° angles. This finally leads to patterns invariant under a rotation of 60°.

4. Conclusion

In this paper, we have presented the first experimental study carried out in an extended geometry of the Rayleigh–Taylor instability of a thin viscous film spread on solid surface. We have observed that the nonlinear growth of this instability leads to the formation of two-dimensional patterns exhibiting different symmetries: 'rolls', hexagonal, axisymmetric, annular of sixfold symmetry. The preferred symmetries are the hexagonal and axial ones, but the other patterns can, however, be forced at small t before relaxing towards the hexagonal system. Starting from the lubrication hypothesis, we have derived the evolution equation of the interface. We have shown that the nonlinearities introduce a second-order term in the amplitude equations that results from the non-invariance of the system under amplitude reflection. By means of rather simple calculations, we have shown that these quadratic terms explain the dominant nature of the hexagonal and axial symmetries. We have also shown that an axisymmetric–hexagonal transition seems to be possible, the intermediate patterns (annular of sixfold symmetry) involving superpositions of 'Bessel patterns': $J_0(qr)$, $J_6(qr)\cos(6\theta)$, $J_{12}(qr)\cos(12\theta)$....

All these results deal with the behaviour at short time. We have, however, given a qualitative analysis of the dripping that we have observed at the latest stage of the instability. Our argument leads to a critical Bond number $B_c = (e_0/\lambda_c)^2 \approx 0.04$ above which the final drops should spontaneously fall, the pendant drops remaining stable below this threshold. In fact, we have observed that even for $B < B_c$ drops still fall after coalescence between two pendant drops. This secondary instability of the drops system obtained at large times deserves further investigation.

Another interesting aspect of our results is the observed evolution of the spatial extent of the patterns. This phenomenon is obvious on figures 5, 7, 8 and 9. The patterns are in fact nucleated in particular regions of the viscous pancake and progressively invade the system. All the calculations made in §3 apply to infinitely extended patterns and neglect this effect. A numerical study of this 'propagation effect' is in progress (see Mitescu, Limat & Wesfreid 1990). A first theoretical discussion can be found in Fermigier *et al.* (1991) together with a short version of the present article. More recent data on the propagation effect, and on dripping processes are also to be published (Limat *et al.* 1992).

After the completion of this work, we became aware of a previous theoretical study of film instabilities (Hynes 1978) that included the case of the thin layer

Rayleigh–Taylor instability. The results of this study agree with ours, except for the J_0 patterns, whose growth was numerically found to dominate that of the hexagonal patterns. This discrepancy remains to be discussed. We thank H. K. Moffatt for having provided us with a copy of this work.

We have benefited from very helpful discussions with I. Mutabazi, J. C. Nataf and J. Prost. This work has received support from the DBT Program 1989 of the National Institute of Universe Sciences (INSU) of France. One of us (M.F.) acknowledges support from the National Science Foundation and the Centre National de la Recherche Scientifique (NSF-CNRS contract n° 920075).

REFERENCES

Abramowitz, M. & Stegun, I. A. 1964 *Handbook of Mathematical Functions.* Dover.

Babchin, A. J., Frenkel, A. L., Levich, B. G. & Sivashinsky, G. I. 1983 *Phys. Fluids* **26**, 3159.

Batchelor, G. K. 1967 *An Introduction to Fluid Dynamics.* Cambridge University Press.

Benney D. J. 1966 *J. Math. Phys.* **45**, 150.

Berenson, J. 1962 *Intl J. Heat Mass Transfer* **5**, 985.

Boudouvis, A. G. & Scriven, L. E. 1990 *J. Magn. Magn. Mat.* **85**, 155.

Brown, H. R. 1989 *Phys. Fluids* A **1**, 896.

Busse, F. H. 1978 *Rep. Prog. Phys.* **41**, 1929.

Buzano, E. & Golubitsky, M. 1983 *Phil. Trans. R. Soc. Lond.* A **308**, 617.

Chandrasekhar, S. 1981 *Hydrodynamic and Hydromagnetic Stability.* Dover.

Cloitre, M. 1989 *Agrégation de particules à deux dimensions induite par la capillarité.* Thesis, University de Paris 6.

Cowley, M. D. & Rosensweig, R. E. 1967 *J. Fluid Mech.* **30**, 671.

Dewel, G., Borckmans, P. & Walgraef, D. 1984 In *Chemical Instabilities* (ed. G. Nivcolis & F. Baras), NATO ASI Series C120. Reidel.

Fermigier, M., Limat, L., Wesfreid, J. E., Boudinet, P., Quilliet, C. & Ghidaglia, C. 1991 In *Growth and Form: Non Linear Aspects* (ed. M. Benamar, P. Pelcé & P. Tabling). Plenum.

Gailitis, A. 1977 *J. Fluid Mech.* **82**, 401.

Gauglitz, P. A. & Radke, C. J. 1988 *Chem. Engng Sci.* **43**, 1457.

Haken, H. 1975 *Rev. Mod. Phys.* **47**, 67.

Hammond, P. S. 1983 *J. Fluid Mech.* **137**, 363.

Huppert, H. E. 1982 *J. Fluid Mech.* **121**, 43.

Hynes, T. P. 1878 Stability of thin films. Ph.D. thesis, Cambridge University.

Iooss, G. & Rossi, M. 1989 *Eur. J. Mech.* B **8**, 1.

Jacobs, J. W. & Catton, I. 1988*a* *J. Fluid Mech.* **187**, 329.

Jacobs, J. W. & Catton, I. 1988*b* *J. Fluid Mech.* **187**, 353.

Kuramoto, Y. 1984 *Chemical Oscillations, Waves and Turbulence.* Springer.

Leblond, P. H. & Mainardi, F. 1987 *Acta Mech.* **68**, 203.

Limat, L., Jenffer, P., Dagens, B., Touron, E., Fermigier, M. & Wesfreid, J. E. 1992 *Physica D* (submitted).

Lister, J. R. & Kerr, R. C. 1989 *J. Fluid Mech.* **203**, 215.

Manneville, P. 1988 In *Propagation in Systems Far from Equilibrium* (ed. J. E. Wesfreid, H. R. Brand, P. Manneville, G. Albinet and N. Boccara). Springer.

Mitescu, C., Limat, L. & Wesfreid, J. E. 1990 *Bull. Am. Phys. Soc.* **35**, 2277.

Myshkis, A. D., Babskii, V. G., Kopachevskii, N. D., Slobozhanin, L. A. & Tyupstov, A. D. 1987 *Low Gravity Fluid Mechanics.* Springer.

Nettleton, L. L. 1934 *Bull Am. Petrol. Geol.* **18**, 175.

Nicolson, M. M. 1949 *Proc. Camb. Soc.* **45**, 288.

NORMAND, C. 1984 *J. Fluid Mech.* **143**, 223.

ORON, A. & ROSENAU, P. 1989*a* *Phys. Fluids* A **1**, 1155.

ORON, A. & ROSENAU, P. 1989*b* *Phys. Fluids* A **1**, 1763.

PALM, E. 1975 *Ann. Rev. Fluid Mech.* **7**, 39.

PISMEN, L. M. 1983 *Ann. N.Y. Acad. Sci.* **404**, 135.

SAFFMAN, P. G. & TAYLOR, G. I. 1958 *Proc. R. Soc. Lond.* A**245**, 312.

SAINSON, J. 1989 Contribution à l'étude des transitions rapides de phase. Thesis, University de Paris 6.

SAINSON, J., BARADEL, C., ROULLEAU, M., LEBLOND, J. & HAKIM, V. 1990 In *Proc. Euritherm Seminar 14, Heat Transfer and Major Technological Hazards,* 15–17 May, vol. 1. Louvain-La-Neuve (Belgium).

TAN, M. J. 1986 *J. Fluid Mech.* **170**, 339.

TAYLOR, G. I. 1950 *Proc. R. Soc. Lond.* A**201**, 192.

VALET, T. & WESFREID, J. E. 1989 In *Proc. EuroMech* 240 (ed. D. G. Crighton & F. Mainardi). University of Bologna.

VRIJ, A. 1966 *Discuss. Faraday Soc.* **42**, 23.

WESFREID, J. E. & ALLAIS, D. 1985 *Bull. Soc. Fr. Phys. Suppl.* **57**, 20.

WESFREID, J. E. & ZALESKI, S. 1984 In *Cellular Structures in Instabilities.* Lectures Notes in Physics, vol. **201**. Springer.

WHITEHEAD, J. A. 1988 *Ann. Rev. Fluid Mech.* **20**, 61.

WHITEHEAD, J. A. & LUTHER, D. S. 1975 *J. Geophys. Res.* **80**, 705.

YIANTSIOS, S. G. & HIGGINS, B. G. 1989 *Phys. Fluids* A**1**, 1484.